A&A 474, 763–776 (2007)
DOI: 10.1051/0004-6361:20066691

Astronomy & Astrophysics

Stellar population gradients in bulges along the Hubble sequence⋆

II. Relations with galaxy properties⋆⋆

P. Jablonka[1], J. Gorgas[2], and P. Goudfrooij[3]

[1] Observatoire de l'Université de Genève, Laboratoire d'Astrophysique de l'École Polytechnique Fédérale de Lausanne (EPFL), 1290 Sauverny, Switzerland
[2] Dpto. de Astrofísica, Facultad de Físicas, Universidad Complutense de Madrid, 28040 Madrid, Spain
[3] Space Telescope Science Institute, 3700 San Martin Drive, Baltimore, MD 21218, USA

Received 3 November 2006 / Accepted 2 June 2007

ABSTRACT

We present the analysis of the radial gradients of stellar absorption lines in a sample of 32 bulges of edge-on spiral galaxies, spanning nearly the full Hubble sequence (from S0 to Sc types), and a large range of velocity dispersion (from about 60 to 300 km s^{-1}). Different diagnostics such as index–index, gradient–gradient diagrams, and simple stellar population models are used to tackle the origin of the variation of the bulge stellar population. We find that the vast majority of bulges show older age, lower metallicity and higher [α/Fe] in their outer regions than in their central parts. The radial gradients in [Fe/H] are 2 to 3 times larger than in Log(age). The relation between gradient and bulge velocity dispersion is interpreted as a gradual build up of the gradient mean values and their dispersions from high to low velocity dispersion, rather than a pure correlation. The bulge effective radii and the Hubble type of the parent galaxies seem to play a more minor role in causing the observed spatial distributions. At a given velocity dispersion, bulges and ellipticals share common properties.

Key words. galaxies: abundances – galaxies: bulges – galaxies: formation – galaxies: evolution – galaxies: stellar content – galaxies: spiral

1. Introduction

Combining results of several recent studies of galaxies of different Hubble types, it seems clear that a proper understanding of bulges of spiral galaxies is crucial to galaxy formation in general. It has been realized that early-type (cD to E/S0) galaxies harbor a variety of luminosity profiles, which has been interpreted as being due to a varying contribution of a disk component (Saglia et al. 1997; de Jong et al. 2004). Bulges have been envisaged as former ellipticals which reacted to the presence of disk accreted later on (e.g., Barnes & White 1984). Other studies have advocated for a "secular evolution" scenario to build bulges, gradually inflating them using disc material (e.g., Sheth et al. 2005 and references therein). For all such studies, one faces the fact that the light distribution of (large) galaxies is dominated by two components, bulge and disk (Allen et al. 2006). While total disk magnitudes vary by ∼2 mag along the Hubble sequence (taking the faintest or brightest extremes of the distribution at each Hubble type), the bulge's ones vary by twice this amount (Simien & de Vaucouleurs 1986; de Jong 1996), i.e., properties of bulges are key to our understanding of the nature of the Hubble sequence.

With the exception of the Milky Way and M31, in which we can resolve individual stars (Sarajedini & Jablonka 2005; Olsen et al. 2006), studies of bulges have to deal with integrated properties of stellar populations. Despite the prospect of yielding crucial information on galaxy formation and assembly history scenarios from analyses of their properties, bulges have received significantly less attention than E and S0 galaxies. This is likely a direct consequence of the considerable challenge of avoiding possible disk light contamination.

Spectroscopic studies of the metallicity and age of the central parts of bulges were pioneered by Bica (1988). During the following several years, clear evidence was provided for a central metallicity–luminosity ($Z - L$) relation. Several studies underlined the similarities between ellipticals and bulges (Jablonka et al. 1996; Idiart et al. 1996), both with respect to the slope of the $Z - L$ relation and to the similar apparent α-element overabundances (relative to solar abundance ratios) in the two types of systems. The Hubble type of the parent galaxy appeared to have little influence on the stellar population properties of the bulge, which instead scaled mainly with central velocity dispersion and bulge luminosity (Jablonka et al. 1996).

A few years later, possible distinctions were suggested between bulge properties of late-type spirals vs. those of early-type spirals (Falcón-Barroso et al. 2002; Proctor & Sansom 2002). As pointed out by Thomas & Davies (2006) however, these apparent differences seem to disappear when the appropriate range of central velocity dispersion is considered (in particular at low values). It is also likely true that the homogeneity of the samples and their sizes have an impact on the conclusions.

An important limitation to our understanding of bulge properties is that virtually all previous spectroscopic studies only sampled the light in the central regions which can easily be significantly affected by disk light, especially for late-type spirals.

⋆ Based on observations collected at the European Southern Observatory, proposals number 58.A-0192(A), 59.A-0774(A) and 61.A-0326(A).

⋆⋆ Figure 6 and full Table 1 are only available in electronic form at `http://www.aanda.org`

Substantial progress would be enabled with spatially resolved spectroscopy of bulges, so that radial gradients of their stellar population can be measured. Unfortunately, investigations of such radial gradients using large surveys have so far only addressed early-type galaxies i.e., elliptical and lenticular galaxies, with only very modest and rare excursions into the case of later type galaxies (e.g., Sansom et al. 1994; Proctor et al. 2000; Ganda et al. 2006; Moorthy & Holtzman 2006).

In order to assess the extent of the similarities between ellipticals and bulges of spiral galaxies and to evaluate to what extent disk material may be influencing the formation and evolution of bulges, we have undertaken a very deep spectroscopic survey of bulges in a large, homogeneous sample of spiral galaxies spanning most of the Hubble sequence.

The galaxy sample, the data reduction procedures and the indices are presented in detail in Gorgas et al. (2007, hereafter Paper I). We present the analysis of the line index radial changes in the current paper. It allows one at last to establish (or discard) the existence of scaling relations and their intrinsic dispersion, and to shed some light on the origin of the spatial variation of the stellar populations within bulges.

2. The sample

We selected a sample of 32 genuine (or close to) edge-on spiral galaxies. As shown in Paper I, 26 galaxies are inclined by 90 degrees, 6 galaxies have lower inclinations (60, 67, 75, 80 and 88 degrees). Galaxies in the northern hemisphere were selected from the Uppsala General Catalog (1973), while southern galaxies were selected from the ESO/Uppsala catalog (Lauberts 1982). Hubble types range from S0 to Sc, with the following frequencies: 7 S0, 4 S0/a, 2 Sa, 4 Sab, 9 Sb, 5 Sbc, and 1 Sc. Their radial velocities range from 550 to 6200 km s^{-1}. Due to the high inclination of the galaxies, a precise morphological classification is difficult. Therefore, we assign an uncertainty of about one Hubble type, which is a fair representation of the catalog-to-catalog variations for a given galaxy.

Part of the spectroscopic observations were conducted at the 2.5 m Isaac Newton Telescope (INT) of the Isaac Newton Group of telescopes on the island of La Palma (Spain). For the southern galaxies we used the 3.6-m ESO telescope and 3.5-m New Technology Telescope (NTT), both at ESO La Silla observatory (Chile). The spectrograph slit was oriented along the minor axis of the bulges.

The recent work of Moorthy & Holtzman (2006) is the closest to the present study. The size of their sample is similar (38 galaxies vs. 32) and they also took care to span a large range of Hubble types. However, Moorthy & Holtzman's sample is composed of galaxies with any inclination angle, and only about ten of them are really close to edge-on. This leads Moorthy & Holtzman to investigate the transition between bulge and disk populations, whereas we totally focus on the intrinsic bulge properties. The depth of the observations is also different: our spectra reach bulge regions at galactocentric distances $\gtrsim$3 times larger in radius than theirs.

3. The line-strength indices

Our analysis is based on the measurements of line-strength indices in the Lick/IDS system (e.g., Worthey et al. 1994; Worthey & Ottaviani 1997). For the sake of a robust determination of the radial variations of the stellar population by overcoming the noise in some individual indices at faint surface brightness level (as in the bulge outskirts), we introduce a few new indices that are linear combinations of some classical Lick/IDS ones. They are listed below:

$\langle$Fe$\rangle$ = Fe2 = (Fe5270+Fe5335)/2; the classical mean Fe index.

Fe3 = (Fe4383+Fe5270+Fe5335)/3; first introduced by Kuntschner (2000).

Fe4 = (Fe4383+Fe5270+Fe5335+Fe5406)/4 ; a composition of indices dominated by Fe lines (see e.g. Worthey 1998 for the chemical content of the individual indices).

Fe5 = (Ca4455+Fe4531+Fe5015)/3; based on indices dominated by a mixture of metals, including α elements.

Fe6 = (Ca4455+Fe4531+Fe5015+Fe5709+Fe5782)/3; an extended "mixed" composite Fe index. It could only be measured in galaxies observed with the 3.6 m ESO telescope (see below).

H_A = (Hδ_A+Hγ_A)/2 and H_F = (Hδ_F+Hγ_F)/2 ; two composite H indices.

Balmer = (Hδ_A+Hγ_A+Hβ)/3; a composite Balmer index, only useful for regions free of emission lines, since Hβ is included.

In order to be consistent in our fitting procedures, we use the same units for all indices, converting the index I into the magnitude index I' by:

$$I' = -2.5 \log\left(1 - \frac{1}{n}\sum_{k=1}^{n} I_k/\Delta l_k\right)$$

where n is the number of indices that compose the total index I and Δl_k is the width (in Å) of the central passband in which the index I_k is measured. Gradients in atomic indices are more linear with galactocentric radius when working with I' than with I. Another advantage of this strategy is that the values of all the indices are comparable with one another, since we are normalizing by the bandpass width.

We end up with a grand total of 33 different indices. Because the observations were done on different telescopes and spectrographs, the wavelength coverage of the spectra is not totally uniform among galaxies. In particular, indices redder than 5600 Å (i.e., Fe5709, Fe5782, Na5895, TiO_1, and TiO_2) could be measured only for the 7 galaxies that were observed at the ESO 3.6 m telescope. We refer the reader to Paper I for a complete description of the conversion of the indices to the Lick/IDS system.

4. The gradients

4.1. Gradient measurements

For each galaxy, the final radial sampling (i.e., the number of bins along the minor-axis radius) is a function of signal-to-noise ratio (S/N). Spatial rows of the 2D spectra were summed until a minimum signal-to-noise of 10 per spatial bin was reached. This procedure did not concern the central parts, where the S/N values were much higher even in a single spectrum row. At the end of this procedure, a set of 1D spectra was associated with each galaxy, along with their corresponding distances to the galaxy centre.

Bulge minor axis effective radii ($r_{\rm eff}$) were derived for all bulges as explained in Paper I. As illustrated in Figs. 1 and 2, our spectra reach the bulge effective radius for all our sample galaxies. For 25% of the sample, we reach 3 $r_{\rm eff}$ and for another 25%, we could reach 10 $r_{\rm eff}$. In order to render the radial gradients fully comparable from one galaxy to another, we scaled all galactocentric distances by these effective radii,

$$I' = A \log(r/r_{\rm eff}) + B.$$

Radial gradients were derived by taking into account both sides of the galaxy minor axes, avoiding dubious measurements such

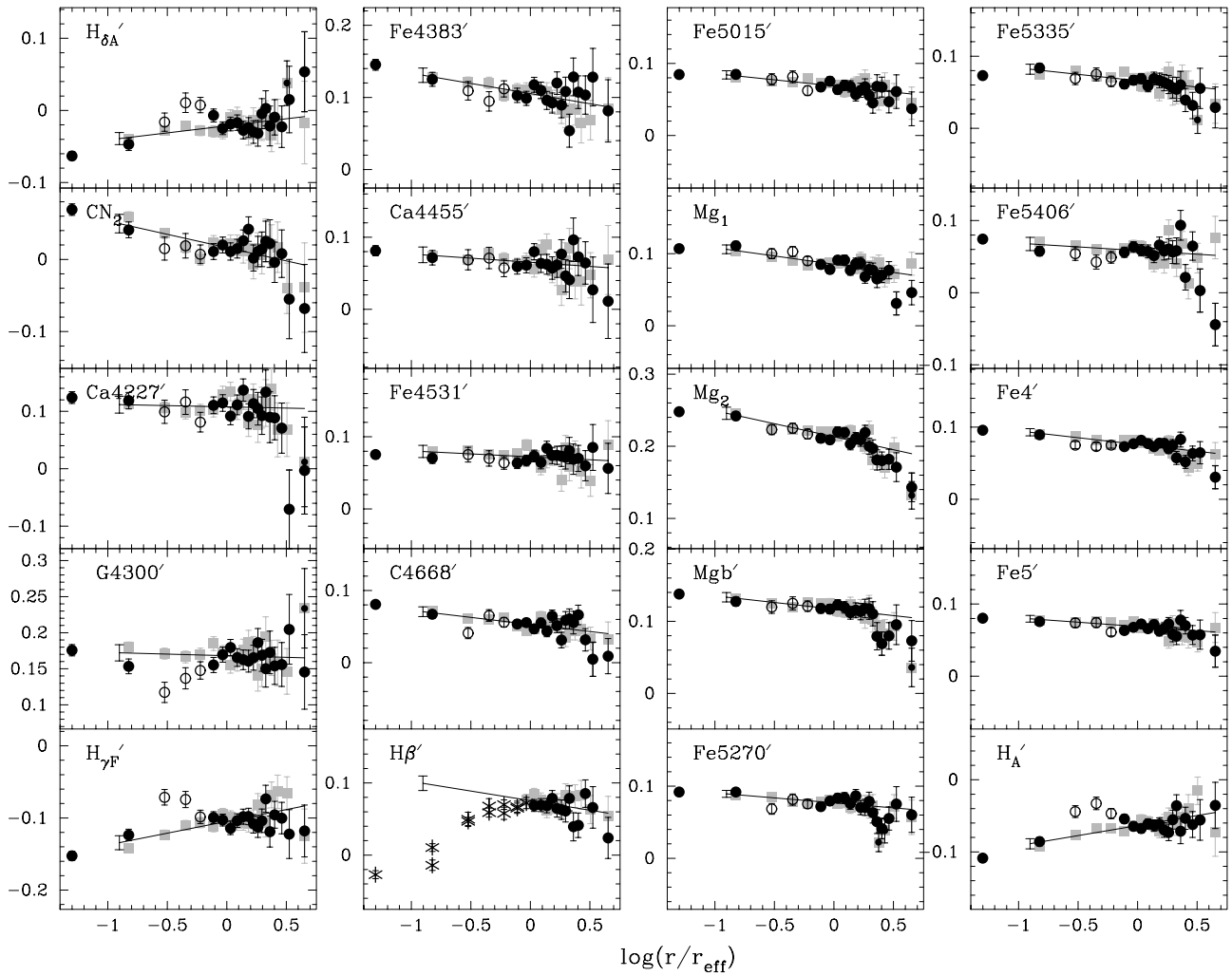

Fig. 1. Radial variation of a sample of 20 spectral indices for NGC 3957. Both sides of the galaxy minor axis are represented by gray squares and black circles for positive and negative radii, respectively. The dust lane is identified with open symbols. Dubious data are indicated by a star. Indices have been measured at the resolution of the Lick/IDS system.

Table 1. For each of our sample galaxy, the 33 measured gradients (first line) and their attached errors (second line) are presented. The full table is accessible along with the electronic version of this paper.

NGC 585	Hδ_A'	Hδ_F'	CN1	CN2	Ca4227′	G-band	Hγ_A'	Hγ_F'	Fe4383′	Ca4455′	Fe4531′
	−0.0086	0.0083	−0.0216	−0.0165	−0.0304	−0.0488	0.0395	0.0292	−0.0208	−0.0001	−0.0176
	0.0245	0.0255	0.0197	0.0198	0.0340	0.0136	0.0135	0.0216	0.0170	0.0167	0.0132
	C4668′	Hβ′	Fe5015′	Mg$_1$	Mg$_2$	Mgb′	Fe5270′	Fe5335′	Fe5406′	Fe5709′	Fe5782′
	−0.0215	−0.0459	−0.0205	−0.0180	−0.0360	−0.0189	−0.0132	−0.0238	−0.0131	−0.0101	−0.0087
	0.0116	0.0331	0.0094	0.0065	0.0064	0.0071	0.0075	0.0078	0.0109	0.0062	0.0130
	Na5895′	TiO1	TiO2	⟨Fe⟩′	Fe3′	Fe4′	Fe5′	Fe6′	H$_A'$	H$_F'$	Balmer
	−0.1275	−0.0013	0.0056	−0.0186	−0.0202	−0.0184	−0.0133	−0.0116	0.0155	0.0188	−0.0341
	0.0194	0.0045	0.0053	0.0061	0.0078	0.0067	0.0072	0.0053	0.0162	0.0195	0.0308

as those placed at the edges of the CCD, excluding locations in the dust lanes, locations affected by emission lines, as well as the inner 0.5−1 arcsec (depending on the slit width) as they could be affected by disk light and seeing effects. The limits of the dust-obscured zone, translated in a decrease in luminosity along the slits, have delineated the edges of the dust lanes.

We adopted an error-weighted least-squares linear fit to the data, with a two-iterations procedure to reject points falling beyond 5σ from the mean relation. The gradients for our 33 indices and 32 galaxies is accessible with the electronic version of this paper. Table 1 provides an example of its format.

An example of the resulting gradients is presented in Fig. 1 for NGC 3957 and a subset of 20 indices. The plain lines indicate the fitted gradients and the error bar at the left edge of the line shows the residual standard deviation of the fit. Figure 2 displays the radial profile of the Mg_2 index for the full sample of galaxies and gives an idea of the variety of gradients. Galaxies like NGC 5084, which represents the most extreme case, flatten in the inner regions. For most galaxies, however, a radial linear variation of the indices with radius is a very fair representation.

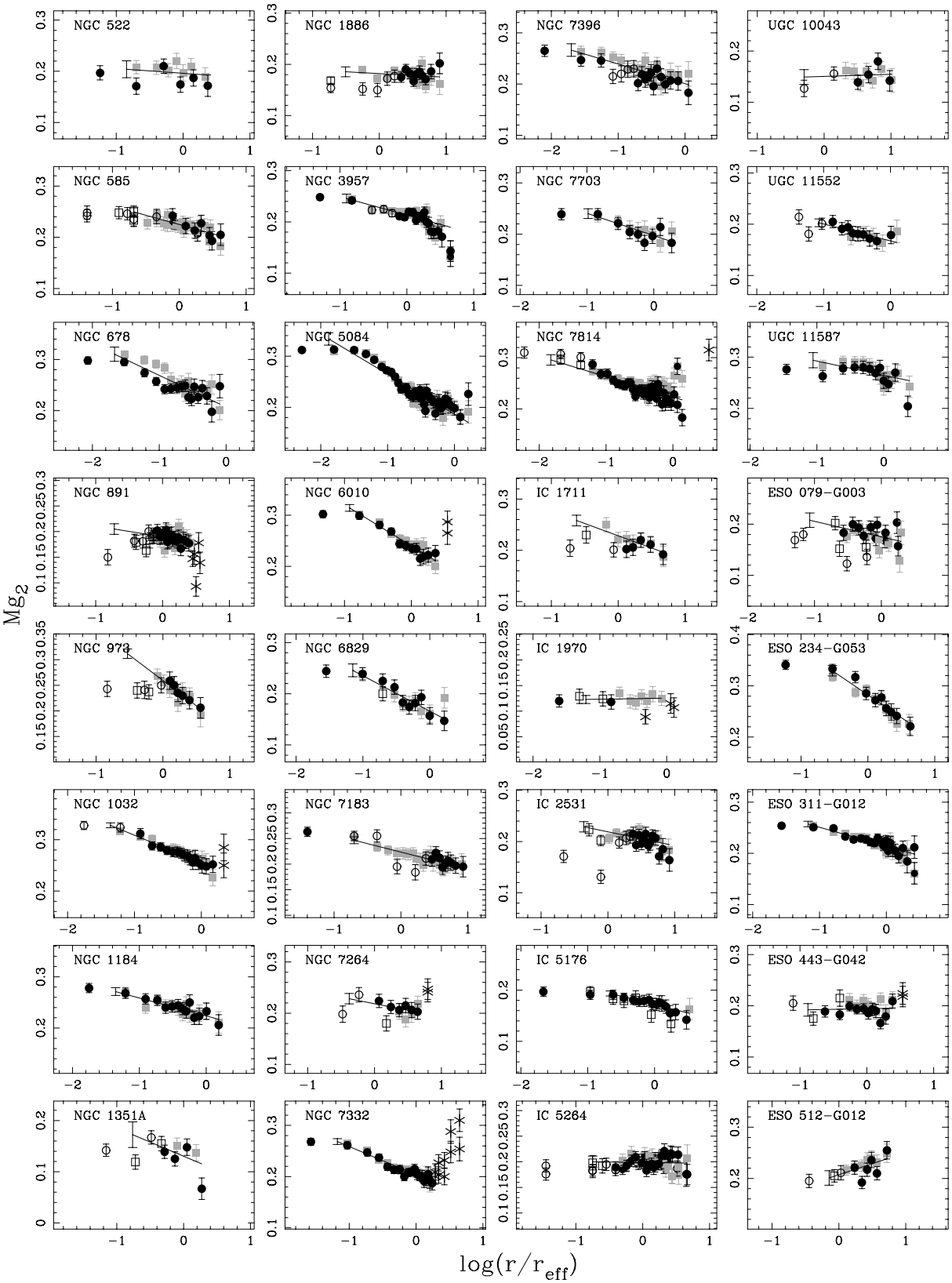

Fig. 2. The radial change of Mg_2 for the full sample of galaxies. Symbols are the same as in Fig. 1.

4.2. Gradient amplitudes and statistics

Figure 3 presents the distribution of the gradient amplitudes for our main indices. The values of the atomic gradients are small relative to past studies due to the logarithmic scale we are using. However, as seen in Fig. 1, the indices can vary by 30 to 50% from the central to the outer bulge regions. The vast majority of the galaxies exhibit negative gradients in all indices (except for the ones involving Balmer lines), i.e., the absorption features increase in strength towards the centre of the bulges. The

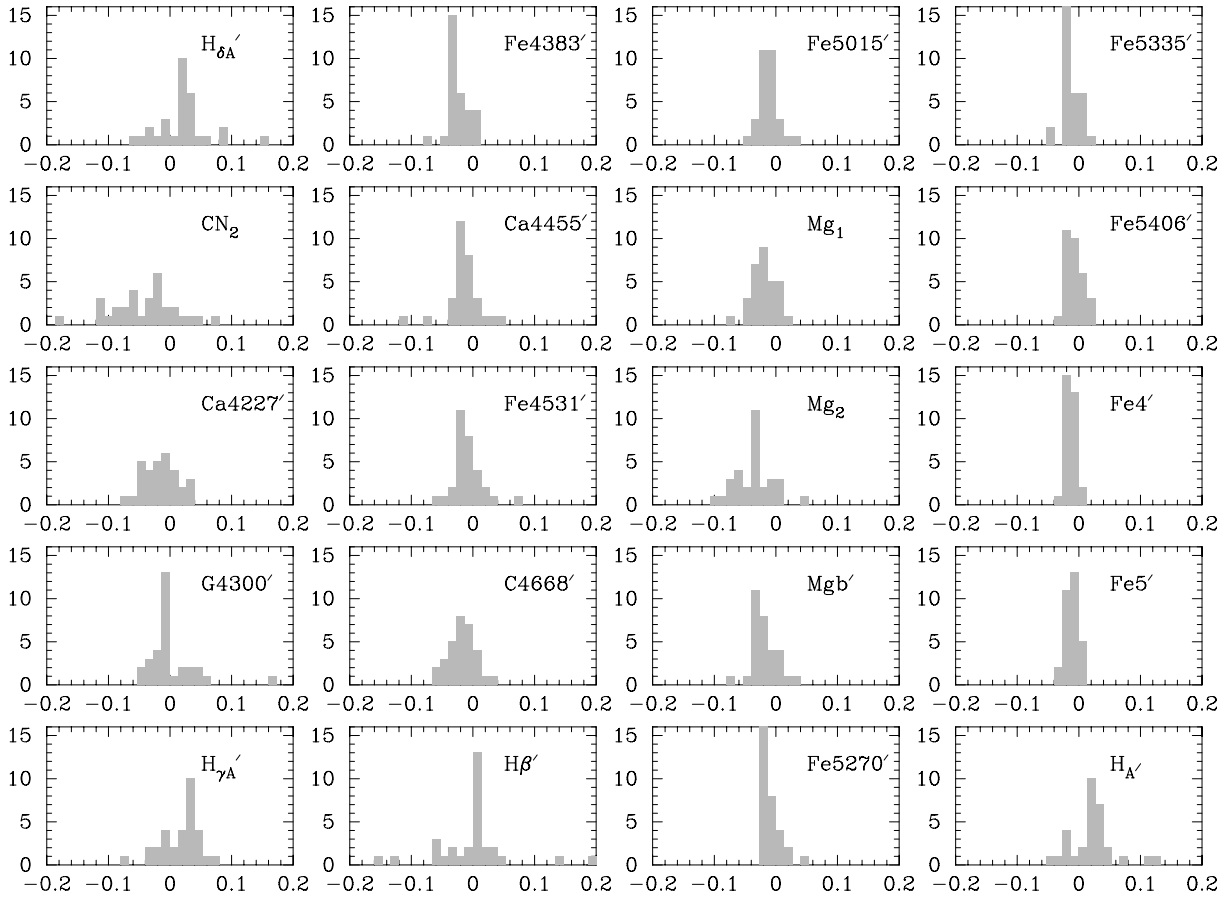

Fig. 3. Histograms (direct bining) of the gradient amplitudes. The x-axis has been chosen such that the extreme values of the gradients could be seen and that all indices could be compared.

range of gradient amplitudes is quite similar from one index to the other. Another interesting feature of Fig. 3 is that, despite a non-negligible dispersion, the distributions are nearly always well peaked, suggesting that some factor other than randomness is at the origin of the spatial distribution of the bulge stellar population properties.

Table 2 gives the error-weighted mean gradients and the dispersion of their distributions for our 33 indices. A comparison between the mean values (Col. 2) and their attached errors (Col. 3) demonstrates that the negative values of the gradients are significant. The dispersions of gradients among galaxies are also significant and not due to observational errors as indicated by the intrinsic dispersions. This means that there is a variety of stellar populations in bulges and an intrinsic diversity in their spatial variation, the origin of which we will try to unveil.

The dispersion around the mean gradient amplitudes ($\sigma_{\rm rms}$) decreases with redder indices (i.e., those measured in the redder part of the bulge spectrum). While this is partly due to the measurement errors which get smaller at larger wavelength, this cannot fully explain the measured dispersions, as can be inferred from the intrinsic ones. The indices which measure a given class of chemical elements (i.e., α elements, iron, CNO) present similar intrinsic dispersions. At this stage, it is difficult to identify the origin of the differences in intrinsic dispersion between the different indices. They can have two and possibly mixed origins: varying ratios of the different chemical species, but also, at least partly, difference in the dynamics of the indices, i.e. their relative sensitivity to changes in abundance or age.

5. The scaling relations

As seen in the previous section, bulges, in general, do exhibit radial changes in their stellar population properties: their central indices are the strongest. In this section, we investigate whether the strength of the gradients scales with some structural parameters or dynamical properties of the bulges.

5.1. The existence of the gradient-σ_0 relation

Figure 4 presents the relation between the gradient amplitude and the bulge central velocity dispersion (σ_0, in km s^{-1}), calculated in a 2″-radius aperture. The solid lines indicate the error-weighted least-square linear fits:

$$\frac{\Delta I'}{\Delta \log(r/r_{\rm eff})} = A \log(\sigma_0) + B.$$

Table 3 provides the coefficients A and B, along with the error-weighted standard deviation σ. In order to evaluate the significance of the fits, we performed an F-test which checks the validity of the assumption of a description of the data by a flat relation fixed to the mean of the gradients. It compares the variance of the distribution implied by such an assumption to the observed one. The smaller the probability returned by the F-test, the more different the distributions. We also used the Spearman test, which qualifies the significance of the correlation between the gradients and σ_0. This test does not take the observational errors into account. This is why we use two independent statistical tests. The smaller the Spearman probability, the more significant

Table 2. Statistics of the gradients for our set of indices. Column (2): error-weighted mean values of gradients; (3): dispersion around the mean; (4): expected dispersion from the errors; (5): intrinsic dispersion.

Index	Mean	$\sigma_{\rm rms}$	σ	$\sigma_{\rm int}$
	(2)	(3)	(4)	(5)
$H\delta'_A$	0.0236	0.0218	0.0123	0.0180
$H\delta'_F$	0.0159	0.0204	0.0149	0.0140
CN_1	−0.0618	0.0335	0.0126	0.0310
CN_2	−0.0635	0.0359	0.0154	0.0325
Ca4227′	−0.0084	0.0148	0.0156	
G4300′	−0.0135	0.0183	0.0123	0.0135
$H\gamma'_A$	0.0339	0.0174	0.0095	0.0146
$H\gamma'_F$	0.0314	0.0226	0.0111	0.0197
Fe4383′	−0.0265	0.0101	0.0102	
Ca4455′	−0.0162	0.0125	0.0106	0.0067
Fe4531′	−0.0135	0.0108	0.0080	0.0072
C4668′	−0.0295	0.0170	0.0072	0.0154
Hβ′	−0.0039	0.0228	0.0190	0.0125
Fe5015′	−0.0158	0.0083	0.0064	0.0053
Mg_1	−0.0264	0.0157	0.0058	0.0146
Mg_2	−0.0459	0.0205	0.0058	0.0197
Mgb′	−0.0223	0.0127	0.0071	0.0105
Fe5270′	−0.0149	0.0095	0.0066	0.0068
Fe5335′	−0.0166	0.0087	0.0067	0.0055
Fe5406′	−0.0145	0.0097	0.0069	0.0068
Fe5709′	−0.0070	0.0064	0.0080	
Fe5782′	−0.0177	0.0112	0.0107	0.0034
Na5895′	−0.0881	0.0632	0.0146	0.0615
TiO_1	−0.0025	0.0094	0.0060	0.0072
TiO_2	−0.0064	0.0117	0.0062	0.0100
⟨Fe⟩′	−0.0163	0.0069	0.0051	0.0047
Fe3′	−0.0198	0.0075	0.0052	0.0054
Fe4′	−0.0186	0.0070	0.0043	0.0056
Fe5′	−0.0146	0.0076	0.0052	0.0056
Fe6′	−0.0099	0.0052	0.0069	
H'_A	0.0293	0.0177	0.0077	0.0160
H'_F	0.0239	0.0212	0.0093	0.0191
Balmer	0.0202	0.0180	0.0157	0.0088

the correlation between the gradients and the bulge central velocity dispersions. As also shown in Fig. 4, there seems to be no statistically significant variation of the amplitude of the stellar population gradients with the bulge central velocity dispersion, with the exception of the Mg_1 and Mg_2 indices.

Intriguingly, while Mg_1 and Mg_2 (both of which are sensitive to magnesium abundance) vary with σ_0, Mgb does not. This dichotomy between the behavior of Mg_2 and Mgb has already been noticed for elliptical galaxies. Mehlert et al. (2003) concentrate on Mgb gradients in elliptical galaxies with a range of velocity dispersions similar to ours and do not find any correlation. More recently, Sánchez-Blázquez et al. (2006) confirm this absence of correlation. Meanwhile, Carollo et al. (1993) report on the correlation of Mg_2 gradients with σ_0 among elliptical galaxies. Ogando et al. (2005) also observe a relation between the Mg_2 gradients and the velocity dispersions of their galaxies.

If one considers the simple stellar population (SSP) models of Vazdekis (1999) or Thomas et al. (2003), the sensitivity of Mgb′ to age at fixed metallicity (or to metallicity at fixed age) is ∼ half that of Mg_2. Indeed, our Mgb′ gradients are half as large as the Mg_2 ones on average. This is however not sufficient to explain the change in behavior of the two indices. It has to be attributed to the intrinsic properties of the indices and, in particular, to their dependencies to abundances. As a clear illustration of this, four galaxies (UGC 10043, ESO 443-042, ESO 512-012, and IC 1970) do not exhibit any gradient in Mg_1 nor in Mg_2, but they do have significantly negative Mgb′ gradients. In those cases, C4668′ shows no radial change either. Therefore, for those galaxies, the carbon abundance seems to supersede the magnesium sensitivity of the indices Mg_2 and Mg_1. This Mg vs. C balance is seen in a quite spectacular way for these 4 galaxies, but it could play a (likely more subtle) role in other bulges. In any case, the sensitivity to different chemical elements seems to be able to explain the discrepant behavior of the three "magnesium" indices.

The indices primarily sensitive to iron exhibit gradients whose amplitudes seem independent of the bulge velocity dispersion. As can be seen in Table 2, the intrinsic dispersions of these amplitudes are extremely small and leave hardly any room for any variation beyond the one consistent with the uncertainties.

5.2. Building- up the gradient-σ_0 relation

The galaxy Hubble types are color-coded in Fig. 4. All galaxy types span nearly the full range of central velocity dispersions, with the exception of the earliest-type galaxies (E/S0 and S0/a) whose central velocity dispersions do not reach low values.

For the E/S0 to S0/a galaxies in our sample, the measurement errors are extremely small and therefore give an excellent idea of the intrinsic dispersion at fixed velocity dispersion. We find that their gradients are independent of the bulge velocity dispersion, whatever index is considered. The range of Mg_2 gradients in our sample is entirely consistent with that of the compilation of S0 galaxies in Ogando et al. (2005).

If one only considers galaxies of types later than Sa, then the G-band and Fe5406 indices reveal some variation with σ_0 as well as Mg_1 and Mg_2, and the slopes of the relations of the latter two indices with σ_0 are slightly stronger than when the full sample is considered. Therefore, it looks like the Mg_1 and Mg_2 trends seen in the full sample arise mainly from the Sa through Sc galaxy types.

However, rather than interpreting the trends between gradient amplitudes and σ_0 as direct correlations, we find that they are due to the combination of a gradual and differential population of the diagrams together with the dynamical range of the indices (i.e., their intrinsic capacity to reach high values by nature). Rather than a smooth change in gradient amplitude with velocity dispersion, one witnesses a three-step process: (i) At large σ, the dispersion among gradients is large but small gradients are relatively rare. (ii) At smaller σ, the dispersion remains large, but galaxies with very weak gradients appear in larger number. (iii) Finally, at $\sigma \lesssim 125$ km s^{-1}, one finds only bulges with either very weak or no radial variation of their stellar population. These successive regimes are, of course, best seen with indices which have a large dynamical range of such as Mg_1 and Mg_2, but it is likely present in all indices.

Only a few previous studies on gradients included (early-type) galaxies with central velocities below ∼125 km s^{-1} (Gorgas et al. 1997; Sánchez-Blázquez et al. 2006). Just as found here, their low-σ galaxies do have very weak or null gradients. Gorgas et al. (1997) find evidence for their bulges to have shallower gradients than ellipticals. However, they compare systems with very different velocity dispersions. The study of Ogando et al. (2005) notices a decreasing number of E and S0 galaxies harboring steep Mg_2 gradients with decreasing velocity dispersion, which is similar to what we find. Finally, Moorthy & Holtzman (2006) mention that the bulges of their sample showing insignificant gradients in [MgFe] have small

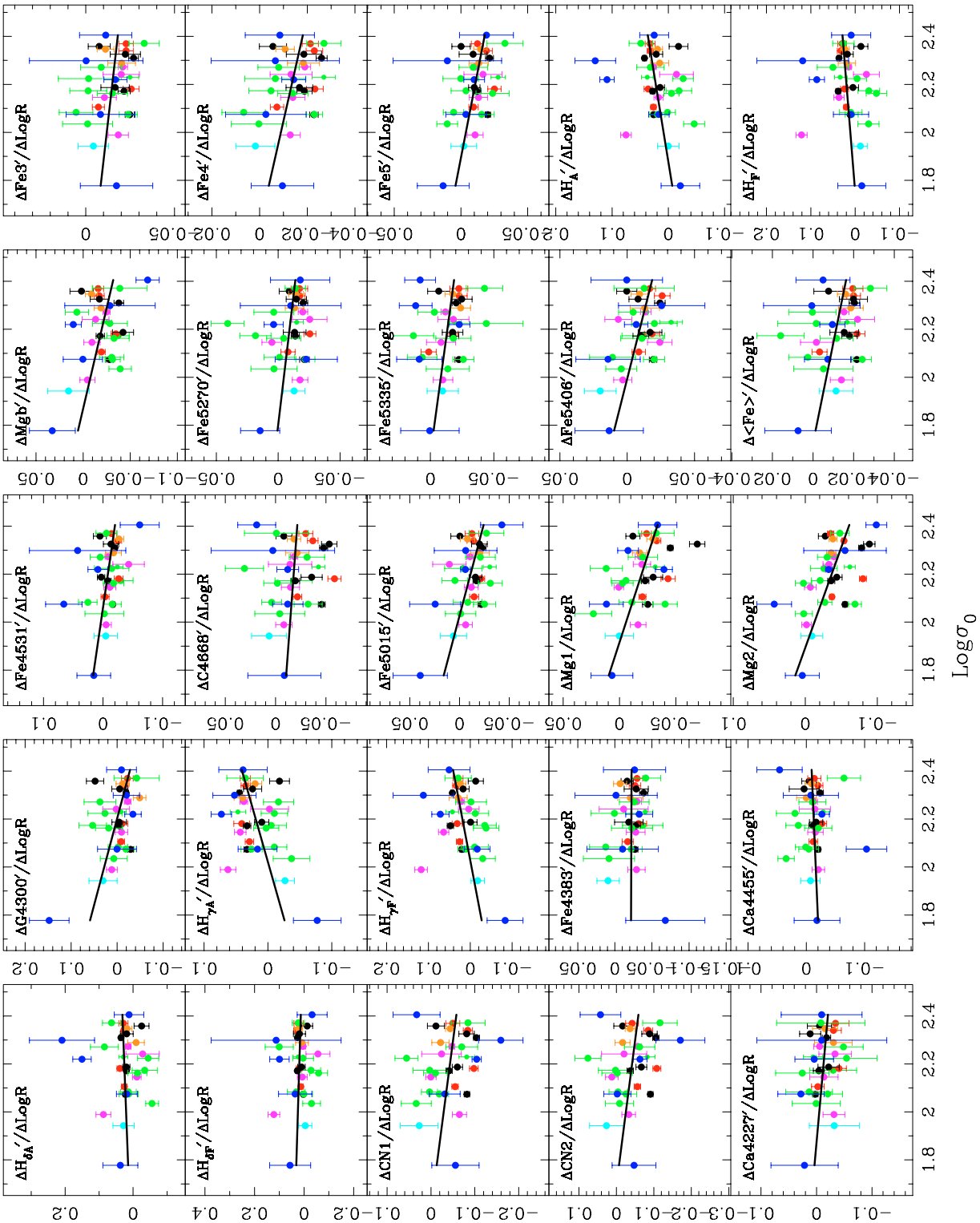

Fig. 4. The relation between the gradients and the bulge central velocity dispersions for the 25 indices that are available for the whole sample of bulges. The color code for the different Hubble types is the following: Black corresponds to E/SO, red to S0/a, orange to Sa, magenta to Sab, green to Sb, blue to Sbc, and cyan to Sc types. The black solid lines show the linear fits.

sizes. Histograms of the distribution of Mg_2 gradients for bulges with $\sigma < 125$ km s^{-1} vs. those with $\sigma \geq 125$ km s^{-1} are shown in Fig. 5. Formally, a Kolmogorov-Smirnov test indicates that the two distributions are different at the 99.95% probability level. We also show a comparison with the elliptical galaxies of Sánchez-Blázquez et al. (2006) which illustrates that Mg_2 gradients disappear at low velocity dispersion in these systems as well.

5.3. Other scaling relations

Mehlert et al. (2003) report on a stronger correlation of absorption line strength gradients with the galaxy velocity dispersion *profiles* than with their central values. We indeed find a correlation, but to a level which is no more significant than with σ_0. This result holds both when considering the full sample and when we restrict our sample to S0 and S0/a galaxies. This is in

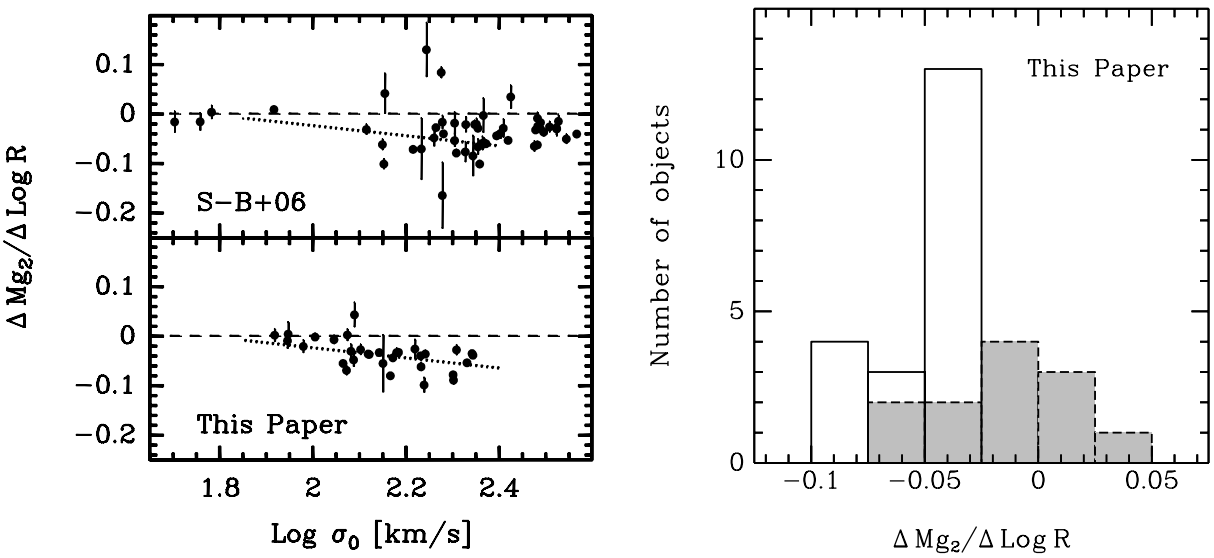

Fig. 5. *Left panels*: the relation between Mg_2 gradient amplitudes and central velocity dispersion for bulges in this paper (lower left panel) and for elliptical galaxies in the sample of Sánchez-Blázquez et al. (2006; upper left panel). To guide the eye, a least-squares fit to the data for the bulges in this paper is plotted as dotted lines in both left panels. *Right panel*: histograms of Mg_2 gradient amplitudes for bulges with central velocity dispersions $\sigma < 125$ km s^{-1} (dashed lines and grey hashing) and with $\sigma \geq 125$ km s^{-1} (solid lines).

Table 3. Linear fits of the variation of the gradients with the bulge central velocity dispersion for the full galaxy sample. *A* stands for the slope of the relations, *B* for their zero points, and σ is the dispersion of the fits. F and S give the probabilities of the F- and Spearman, respectively (see text).

Index	*A*	*B*	σ	F	S
$H\delta'_A$	0.025 ± 0.021	−0.032 ± 0.047	0.02	0.97	0.81
$H\delta'_F$	0.028 ± 0.025	−0.045 ± 0.055	0.02	0.95	0.98
CN1	−0.046 ± 0.022	0.039 ± 0.049	0.03	0.95	0.17
CN2	−0.033 ± 0.026	0.010 ± 0.057	0.04	0.98	0.11
Ca4227′	−0.058 ± 0.026	0.117 ± 0.056	0.02	0.56	0.20
G4300′	−0.036 ± 0.020	0.065 ± 0.044	0.02	0.89	0.02
$H\gamma'_A$	0.042 ± 0.015	−0.059 ± 0.034	0.02	0.83	0.10
$H\gamma'_F$	0.042 ± 0.017	−0.061 ± 0.038	0.03	0.89	0.05
Fe4383′	−0.015 ± 0.015	0.008 ± 0.034	0.01	0.92	0.37
Ca4455′	−0.005 ± 0.017	−0.006 ± 0.036	0.01	1.00	0.65
Fe4531′	−0.021 ± 0.013	0.032 ± 0.028	0.01	0.89	0.06
C4668′	−0.009 ± 0.012	−0.009 ± 0.026	0.02	0.99	0.53
Fe5015′	−0.003 ± 0.011	−0.009 ± 0.025	0.01	1.00	0.08
Mg1	−0.066 ± 0.010	0.121 ± 0.021	0.01	0.49	0.01
Mg2	−0.053 ± 0.009	0.071 ± 0.020	0.02	0.79	0.00
Mg'_b	−0.004 ± 0.012	−0.014 ± 0.026	0.01	1.00	0.42
Fe5270′	−0.009 ± 0.010	0.006 ± 0.023	0.01	0.97	0.33
Fe5335′	−0.008 ± 0.011	0.002 ± 0.024	0.01	0.97	0.15
Fe5406′	−0.019 ± 0.010	0.027 ± 0.023	0.01	0.87	0.08
⟨Fe⟩′	−0.014 ± 0.008	0.015 ± 0.018	0.01	0.88	0.13
Fe3′	−0.014 ± 0.008	0.011 ± 0.018	0.01	0.90	0.15
Fe4′	−0.012 ± 0.007	0.008 ± 0.014	0.01	0.90	0.07
Fe5′	−0.007 ± 0.008	0.002 ± 0.018	0.01	0.97	0.06
H'_A	0.026 ± 0.013	−0.027 ± 0.028	0.02	0.94	0.07
H'_F	0.036 ± 0.015	−0.054 ± 0.033	0.02	0.92	0.16

agreement with the results of Sánchez-Blázquez et al. (2006) for elliptical galaxies. Figure 6 displays the relations between the bulge gradients and their effective radii. Here again, Mg_1 and Mg_2 are the only indices for which a dependence is clearly seen. However, the slopes of the relations are 2−3 times smaller than the ones with σ_0. This holds for all indices. This means that any dependence on the bulge mass is dominated by the effect of the the bulge central velocity dispersion.

6. Index–index diagrams

We now try to understand the nature of the radial gradients in terms of physical quantities such as age and/or chemical abundance variations of the stellar population. We have considered the solar-scaled SSP models of Vazdekis (1999) and the SSP models of Thomas et al. (2003, 2004) which allow α-enhancement variations. The use of these two series of models was meant to assess the robustness of our conclusions. As a matter of fact, we find that they indeed yield the same broad conclusions, and we consequently choose to only present the analysis conducted with the Thomas et al. models which include non-solar [α/Fe] values, and thus offer a more detailed description.

One shortcoming using SSPs is that when directly applied to galactic composite stellar populations, the absolute values of age and metallicity are intrinsically biased, due to the simplified description as "single" stellar populations. They are meant to get close enough to the luminosity-weighted mean quantities. Another problem is the existence of some degeneracies, in particular between [α/Fe] and age for a fair number of indices. For these reasons, we avoid assigning absolute ages or metallicity values to our galaxies.

As mentioned earlier, galaxies can roughly be divided in two categories: Those with significant radial gradients and those without. In the following we address each group separately with the aim of possibly identify differences between them.

6.1. Galaxies with strong gradients

First, we consider galaxies for which Mg_2 and ⟨Fe⟩′ gradients are strictly negative, taking into account their errors (1σ). Mg_2 is a composite index, simultaneously sensitive to metallicity, α-elements, and age. Therefore, this criterion does not select any particular type of galaxy. The criterion on ⟨Fe⟩′ discards 3 bulges, whose gradients, although negative, have large errors. Including them would not help our understanding.

While the Mgb′ vs. ⟨Fe⟩′ diagram is highly degenerate in age and [Fe/H], it does offer a good determination of [α/Fe]. In Fig. 7, for each galaxy, we join with an arrow the central indices

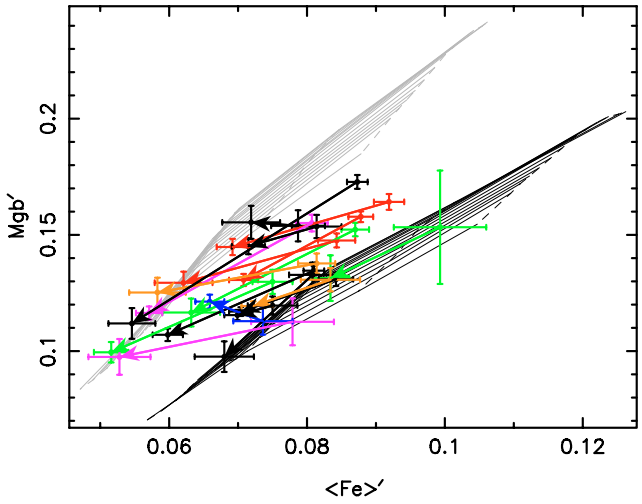

Fig. 7. Index–index diagram for galaxies harboring clear gradients. SSP Model grids are shown for ages running from 15 Gyr to 3 Gyr. The location of [Fe/H] = −0.33, 0.00, 0.35 and 0.67 are identified by dotted lines. At the same time, they indicate the direction of an age variation. The gray and black grids correspond to [α/Fe] = 0.3 and 0.0, respectively. Arrows connect the central indices, integrated in a 4″ aperture, to the values of the indices at the effective radius of the bulge. The galaxy Hubble type color coding is the same as in Fig. 4.

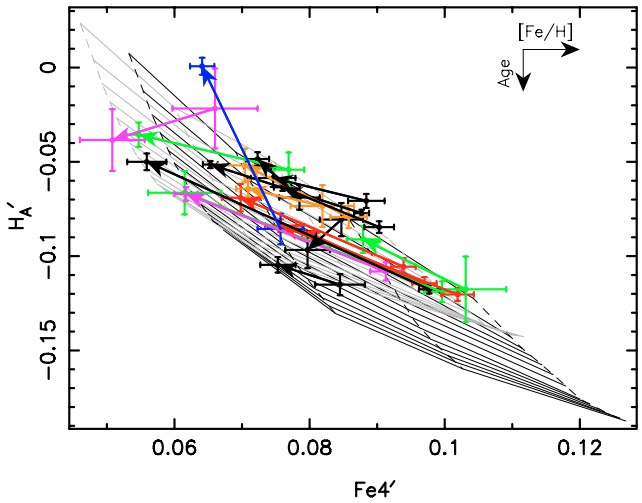

Fig. 8. Index–index diagram for galaxies harboring clear Mg_2 gradients. The two grids of models for [α/Fe] = 0.0 and 0.3 are shown by black and light gray lines, respectively. Ages run from 15 Gyr to 3 Gyr and go along the dashed lines (younger ages correspond to higher H'_A). One Gyr separates two adjacent age lines. Arrows join the central indices, integrated in a 4 arcsec aperture, with the value of the indices at the bulge effective radius. The galaxy Hubble type color coding is the same as in Fig. 4.

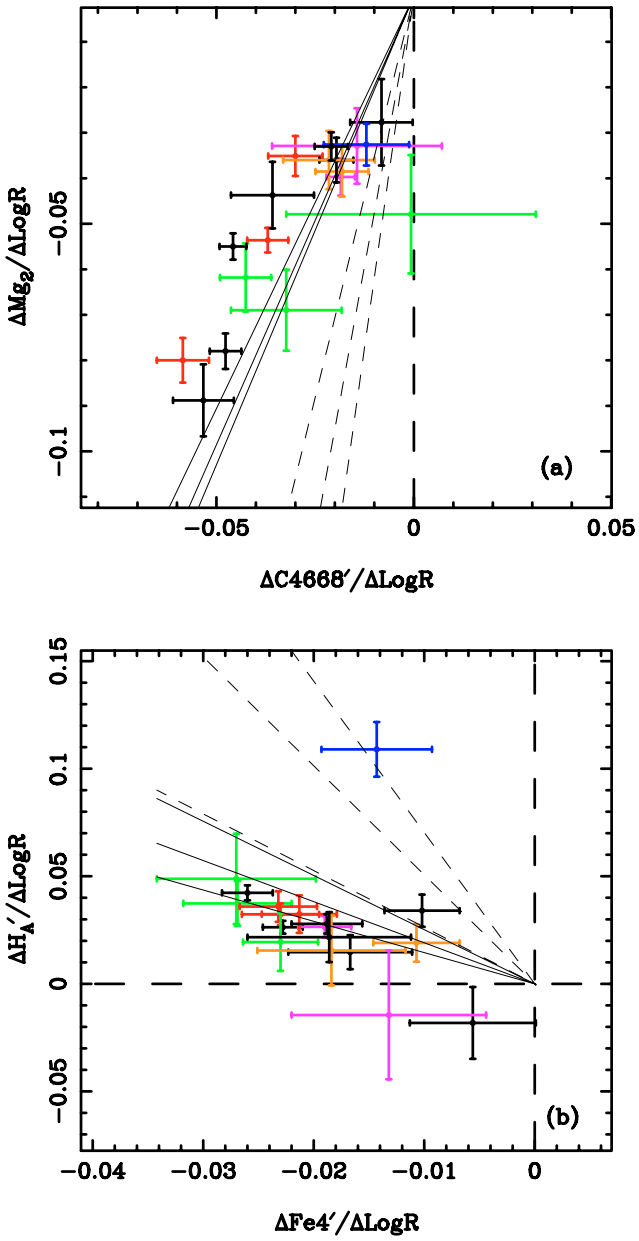

Fig. 9. Gradient–gradient diagrams for galaxies harboring clear Mg_2 gradients. The galaxy Hubble type color coding is the same as in Fig. 4. The direction of variation of the indices with [Fe/H] only, or with age only, is shown by the plain and dashed lines, respectively.

to the indices measured at the bulge effective radius. All galaxies lie within a region delimited by the two lines at [α/Fe] = 0 and [α/Fe] = 0.3 and the two iso-metallicity lines at [Fe/H] values of −0.33 and 0.67. The iso-age lines span the range 3−15 Gyr. As shown by the direction of the arrows, most of the galaxies show both a decrease in metallicities and an increase in [α/Fe] towards larger radii. The variation in [Fe/H] is of the order of 0.3 dex, while it is smaller for [α/Fe] ($\lesssim$0.1 dex). A few bulges seem to harbor pure [α/Fe] or pure [Fe/H] gradients.

Figure 8 presents the variation of Fe4′ as a function of H'_A for our galaxies, superimposed on the same grids of models as mentioned above. Here again, the index gradients are clearly mostly due to metallicity. H'_A gradients are small and positive. An interesting feature is that the longest arrows (i.e., the largest gradients) are located at the bottom of the diagram, implying a slightly older luminosity-weighted mean age. The relative shift is small, of the order of ∼2 Gyr, but the effect seems systematic. Taking into account the increase in [α/Fe] at larger radii revealed by the previous diagnostic diagram, the amount of possible variation due to age corresponds to a few Gyrs at most (often of the order of 1−3 Gyr), the central parts of the bulges being younger than their outer regions. There are three apparent exceptions to this general trend: UGC 11552 and UGC 11587 seem to have stronger age gradients than the bulk of the galaxies, as they have strong negative H'_A gradients. The third galaxy, IC 5176, harbors a strong and positive H'_A gradient. The bulge of this galaxy exhibits gradients in C4668′ and in Mgb′ that are among the

smallest in the sample, while showing a strong radial increase of its high-order Balmer lines towards the outer regions of the bulge. Its outer parts therefore seem indeed younger than the central ones. As a matter of fact, Hα and [N II] emission are present all the way from the central to the outer regions, which increases the uncertainties of both Balmer and Mgb index measurements (e.g., Goudfrooij & Emsellem 1996). Admittedly, we do not see any straightforward explanation for these traces of gas. One possibility is pollution by the disk component, even though IC 5176 does not (currently) have a bar (Chung & Bureau 2004).

Another way to look at the question of the nature of gradients is provided by Fig. 9. The SPP models, plotted in index–index diagrams, show grids from which one can easily derive the amount of variation when only one of the parameters (age, metallicity, or [α/Fe]) is varying.

The advantage of this method is that it is immediately applicable to any radial gradient–gradient observational plot. The slopes associated with expected pure age and pure metallicity variations have been derived for stellar populations of ages between 3 and 15 Gyr and metallicities ([Fe/H]) between −1.35 and 0.67. We considered [α/Fe] = 0.3, given our diagnosis of Fig. 7. The results would change in detail but not in conclusion if we had used [α/Fe] = 0.0. The slope of the metallicity variation depends on the age considered and, conversely, the age variation depends on the range of metallicity considered. For this reason, we show the maximum, mean and minimum slopes. Figure 9, as was Fig. 8, is meant to summarize our investigations. Other sets of indices have been considered, however, we avoid any redundant illustration. The choice of the two sets of indices, (Mg_2, C4668′) and (H'_A, Fe4′) was driven by four criteria: (i) They involve well-measured indices (ii) the index–index model grids are regular, (iii) they show significantly different slopes for age and metallicity changes, and (iv) the diagrams include sensitivities to all three parameters (age, [Fe/H] and [α/Fe]), so that the three can be considered together.

Figure 9 demonstrates clearly that a pure metallicity gradient nearly fully explains the amplitude of the observed gradients. Interestingly, the smallest slopes shown in Fig. 9 fit the data the best (they correspond to the oldest ages). Only one galaxy, IC 5176, is more compatible with a major radial change in age, as discussed above. Here the line passing through the IC 5176 location corresponds to metallicities below solar.

All galaxies do not fall exactly on the models tracing a pure metallicity variation. The residual distances to these lines are compatible with an age and/or [α/Fe] variation. As these two parameters make the indices move in the same direction, it is very hard to distinguish between them using this method, but we already know that likely both can be accounted for, in small proportions.

6.2. Galaxies with weak or no gradients

We define this category of galaxies as bulges whose gradients in Mg_2 are compatible with a null value within the errors. Eight galaxies in our sample fall in this category, i.e., 25 percent of our sample. Their Hubble types are mixed, but no very early-type galaxy is present (2 Sab, 2 Sb, 3 Sbc, 1 Sc). The three Sbc galaxies (UGC 10043, ESO 512-012, NGC 1351A) have large error bars, both in Mg_2 gradients and in $\log\sigma$, essentially due to the restricted number of bins on which the gradients could be evaluated robustly.

As we did for the galaxies with strong gradients, we examine the relation between Fe4′ and H'_A in Fig. 10. All the bulges with

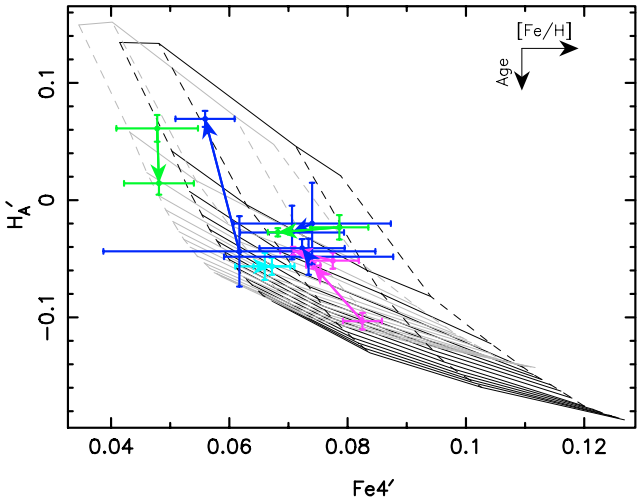

Fig. 10. Index–index diagram for galaxies harboring weak or no Mg_2 gradient. Ages run from 1 Gyr to 15 Gyr. The rest of the symbols and parameters are the same as in Figs. 8 and 4.

weak gradients are shifted to lower metallicities, as compared to the strong gradient ones.

Furthermore, none of these bulges show strong Fe4′ and H'_A. This means that weak gradients are associated with low global chemical enrichment. More precisely, the indices measured at $r_{\rm eff}$ populate a region of the diagram which is very similar to that of the bulges with strong gradients (cf. Fig. 8), but the central index strengths do differ significantly. This supports a scenario where star formation proceeds from the outer to the inner parts, and where the outer bulge regions share universal chemical properties. The difference between bulges arises from star formation in their central regions.

Two galaxies seems to have a large H'_A radial variation. NGC 1351A (the first dark blue arrow on the left side of Fig. 10) has amongst the lowest number of bins available for the fit of its gradients. Despite an apparently impressive change in H'_A, careful consideration of the uncertainties forces us to discard any significant gradient in this bulge. The case of IC 5264 (magenta arrow) is different. Its spectra have high signal-to-noise ratios and its radial sampling is good. As for IC 5176, seen previously, we indeed face a case of younger ages in the outer parts of the bulge. But again, we do not find any straightforward explanation for this galaxy to be different from the bulk of our sample.

The three remaining galaxies, NGC 522, NGC 1886, and ESO 443-042 have null or very weak gradients. They are all well sampled in radius, therefore the absence of spectral radial variation can be considered real and attributable to their small central velocity dispersion and low global chemical enrichment.

6.3. Comparison with elliptical galaxies

The work of Sánchez-Blázquez et al. (2006) gives us the opportunity to compare a set of indices in elliptical galaxies to our data, in a range of velocity dispersion very similar to the one of our sample of bulges. In particular, for our present interest, it allows a look at the relations between the spatial distribution of different indices: they offer clues on the star formation histories in the galactic systems. Figure 11 displays this comparison for gradients in Mg_2, C4668′, Fe4383′ and $H\gamma'_A$. Obviously, the gradients in bulges agree very well with those in elliptical galaxies, both in amplitude and in the relations between sets of gradients.

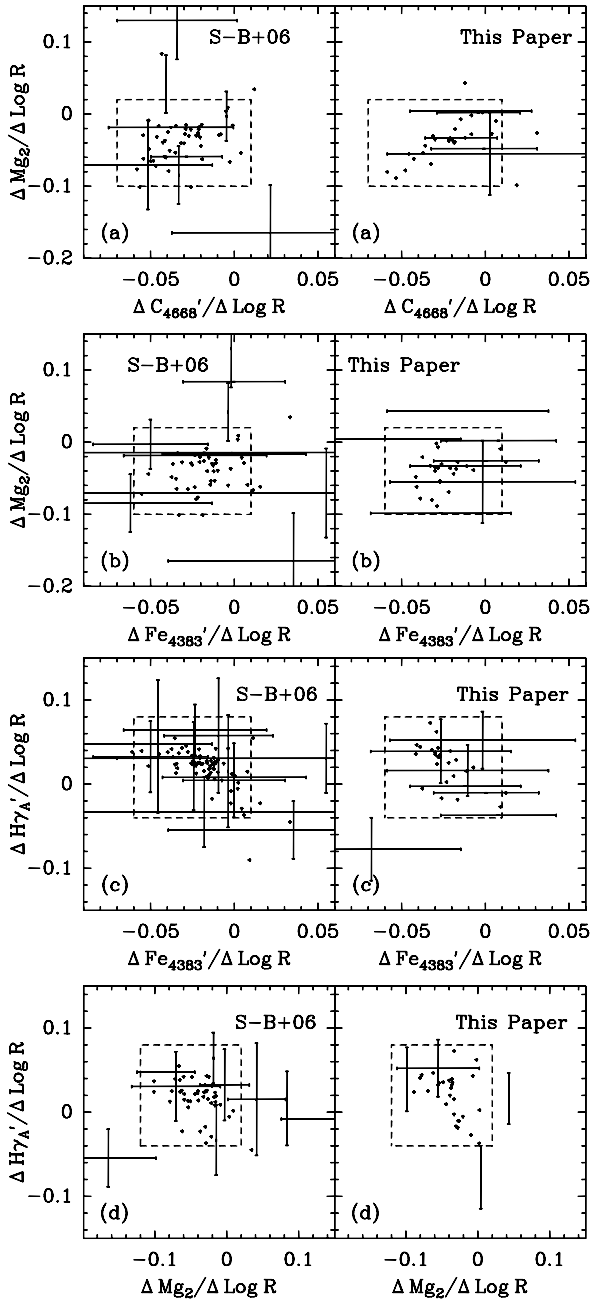

Fig. 11. Comparison of gradients of well-measured indices for bulges in this paper with those for elliptical galaxies in the sample of Sánchez-Blázquez et al. (2006; labeled "S–B+06"). Error bars are only plotted if they exceed 0.03 dex in a given index gradient. For ease of comparison, boxes with dashed lines are drawn in a fixed position for each pair of gradient–gradient plots.

This strengthens further the similarities between the two types of spheroids.

6.4. Quantification

We now try to quantify the [α/Fe], age and [Fe/H] variations between the bulge effective radii and their central parts. We use the models of Thomas et al. (2003, 2004). First, we derive [α/Fe] from the Mgb′−⟨Fe⟩′ diagram. Subsequently and independently, we calculate the age and metallicity, as inferred from the H'_A–Fe4′ plane, at $r_{\rm eff}$ and in the bulge central parts. The ages and metallicities are derived at the computed [α/Fe] values. For those, we have considered initial mean ages of 10 and 5 Gyr, and checked that the dependence of the final age and metallicity variation on this a priori choice was negligible.

Table 4. Variation in [α/Fe], age and [Fe/H] between the bulge bulge effective radii and the central regions. Negative values indicate an increase of the considered quantity.

Galaxy	Δ[α/Fe]	Δ Age	Δ[Fe/H]
NGC 522	0.2 ± 0.1	−0.6 ± 4.0	0.15 ± 0.24
NGC 585	0.1 ± 0.1	1.7 ± 1.8	−0.23 ± 0.16
NGC 678	0.1 ± 0.1	6.1 ± 7.6	−0.85 ± 0.29
NGC 891	−0.5 ± 0.3	2.2 ± 3.5	−1.06 ± 2.24
NGC 973	−0.2 ± 0.1	−6.0 ± 9.5	0.76 ± 2.81
NGC 1032	0.1 ± 0.0	3.3 ± 2.5	−0.51 ± 0.13
NGC 1184	0.2 ± 0.1	2.7 ± 2.9	−0.41 ± 0.13
NGC 1351A	−0.2 ± 0.4	−4.3±14.3	0.00 ± 0.50
NGC 1886	0.0 ± 0.1	0.2 ± 1.3	−0.25 ± 0.26
NGC 3957	0.1 ± 0.0	1.0 ± 0.6	−0.29 ± 0.11
NGC 5084	0.2 ± 0.1	3.6 ± 3.0	−0.88 ± 0.12
NGC 6010	0.0 ± 0.0	2.0 ± 2.6	−0.33 ± 0.12
NGC 6829	0.2 ± 0.1	4.2 ± 2.0	−0.52 ± 0.16
NGC 7183	0.1 ± 0.1	−0.4 ± 1.0	−0.06 ± 0.12
NGC 7264	−0.1 ± 0.2	0.6 ± 5.4	−0.29 ± 0.55
NGC 7332	0.2 ± 0.1	1.1 ± 1.4	−0.17 ± 0.16
NGC 7703	0.0 ± 0.1	1.1 ± 0.8	−0.37 ± 0.16
NGC 7814	0.2 ± 0.0	4.0 ± 3.0	−0.69 ± 0.15
IC 1711	0.0 ± 0.2	0.8 ± 1.7	−0.32 ± 0.23
IC 1970	0.0 ± 0.3	2.8 ± 2.8	−0.32 ± 0.47
IC 2531	−0.1 ± 0.2	−1.0 ± 4.5	0.07 ± 0.40
IC 5176	0.2 ± 0.1	−4.1 ± 2.5	0.22 ± 0.16
IC 5264	0.1 ± 0.1	−4.1 ± 2.4	0.04 ± 0.11
UGC 10043	0.0 ± 0.7	0.4 ± 2.8	−0.16 ± 0.62
UGC 11587	0.1 ± 0.1	6.2 ± 3.6	−0.20 ± 0.20
UGC 11552	0.3 ± 0.1	6.1 ± 4.9	−0.38 ± 0.31
ESO079−003	0.0 ± 0.2	−1.1 ± 6.3	−0.12 ± 0.35
ESO234−053	0.1 ± 0.1	3.0 ± 3.7	−0.12 ± 0.43
ESO311−012	−0.1 ± 0.1	−1.1 ± 1.5	−0.08 ± 0.12
ESO443−042	0.0 ± 0.1	0.7 ± 0.9	−0.42 ± 0.27
ESO512−012	0.1 ± 0.2	−0.1 ± 7.2	0.00 ± 0.77

The results are listed in Table 4. As noticed previously in a qualitative way, the outer parts of the bulges have (with a few exceptions) higher [α/Fe], older ages and lower metallicities than the inner parts. Only two galaxies, IC 5264 and IC 5176, have significant positive age gradients. Note that due to the uneven spacing between the model lines in the H'_A–Fe4′ diagram, the absolute errors attached to variations in age are larger when measured for the oldest populations (for which model lines are close together) than for younger populations. Similarly, the variations themselves are maximized. Therefore, we are effectively measuring upper limits of Δage. This effect does not exist for [Fe/H] for which the grid lines are more evenly separated from one another. The uncertainties in Δ[Fe/H] are mainly linked to the errors in Δ[α/Fe] (besides the observational ones). This is particularly true for galaxies which seem to harbor a positive metallicity gradient. Galaxies having insignificant age gradients also have negligible metallicity gradients. Figure 12 illustrates the results of Table 4 and presents the relations between the variations in [α/Fe], age and [Fe/H] with the bulge central velocity dispersion. The description of the $Mg_2 - \sigma_0$ relation in Sect. 5.2 is applicable here as well. This is particularly true for Δ[Fe/H] which has the largest dispersion: i.e., there isn't any significant correlation between metallicity gradient and velocity dispersion, strictly speaking. Instead one sees a decrease in the range of possible gradient values at lower σ.

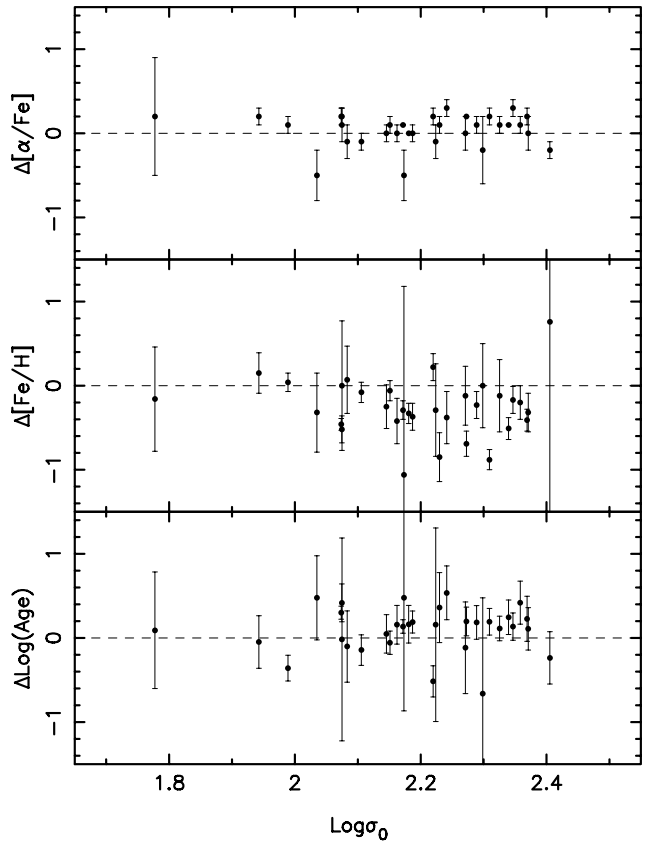

Fig. 12. The relation between ΔLog(Age), Δ[Fe/H], and Δ[α/Fe] with the bulge central velocity dispersion. Δs are measured from the bulge effective radii to the bulge centres

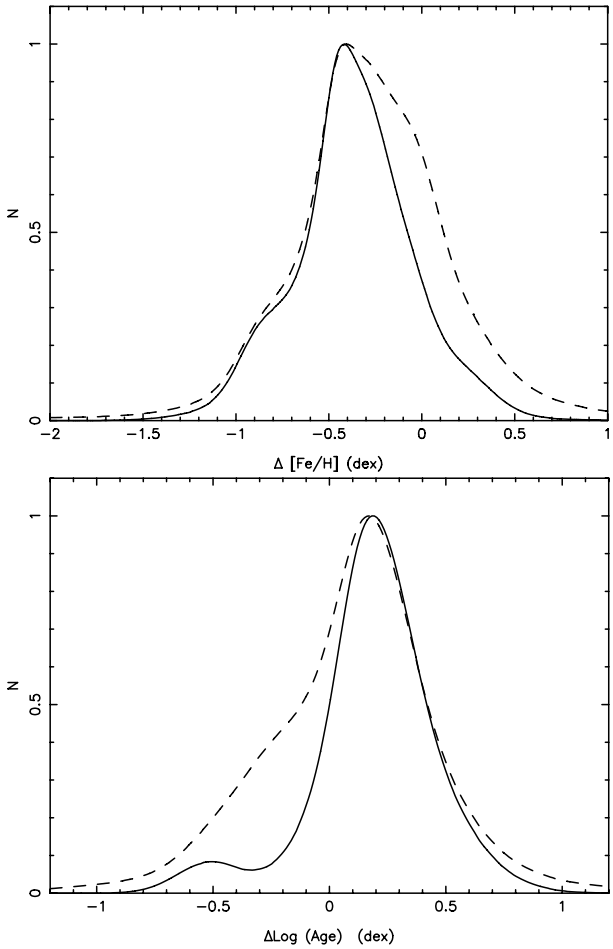

Fig. 13. Generalized histograms of the distribution of radial changes in [Fe/H] and Log(age), calculated between the bulge effective radii and the bulge centre, as tabulated in Table 4. The dotted lines correspond to the full sample of galaxies; the solid lines show the histograms of the galaxies with strong gradients.

In order to quantify the qualitative statement made earlier that bulges have comparable properties at their effective radii, while they differ in their central regions, we measured their mean ages and metallicities. At identical ages, the weak gradient bulges have an error weighted mean [Fe/H]($r_{\rm eff}$) = 0.11 dex, with a dispersion of 0.14 dex. Strong gradient bulges have a mean [Fe/H]($r_{\rm eff}$) = 0.05 dex with a dispersion of 0.19 dex. This must be compared to a mean central metallicity of [Fe/H] = 0.13 dex (dispersion of 0.19 dex) and 0.45 dex, (dispersion of 0.14 dex), for the weak and strong gradient bulges, respectively. Note that these values are derived from SSP models. As such, they are not definite. The comparison they allow between galaxies is however robust. The galactocentric distance of one effective radius is chosen because all our galaxies have spectra of adequate quality there. However, it does not yet sample the most outer bulge regions, where we think there is a lot to learn on the very early stages of bulge formation.

Figure 13 shows the generalized histograms of ΔLog(age) and Δ[Fe/H]. We choose here a logarithmic representation of the age for internal homogeneity (in the sense that index variations scale approximately linearly with Log (age)) and for a more direct comparison with the metallicity scale. Both the full sample, in dashed line, and the strong-gradient galaxy sub-sample, in solid line, are shown. By nature of the use of generalized histograms, the errors are taken into account.

Both the age and the metallicity gradient distributions are very well peaked, at ∼0.15 dex in Log(age) (1.5 Gyr in age) with a dispersion σ = 0.2 dex (in Log(age)) (1.3 Gyr in age), and at −0.4 dex with a dispersion σ = 0.3 dex for [Fe/H]. They correspond to peak values of the gradients of ∼0.07 and ∼−0.2 for the Log(age) and [Fe/H], respectively.

Similarly, the mean gradients for the age and [Fe/H] are 0.06 and −0.16, respectively. In other words, metallicity gradients are two to three times larger than those in age (in log scale). These values are very close to those derived for elliptical galaxies with a comparable range of velocity dispersions by Sánchez-Blázquez et al. (2006, see summary of other analyses therein): 0.082 and −0.206. The different grids of models and relative distribution in velocity dispersion within each sample suffice in explaining the small differences between their and our analyses. Although the distribution of gradient amplitude is more meaningful than their mean values in studying the processes at play in building spheroids, the similarity between mean values of gradients in ellipticals and bulges suggests that they must share a fair amount of common formation history.

7. Conclusions

We have presented the analysis of radial gradients of stellar absorption line strengths in a sample of 32 edge-on spiral galaxy bulges. The sample galaxies span nearly the full Hubble sequence (from S0 to Sc types), and have a large range of dynamical properties, with their bulge central velocity dispersions

ranging from ~60 to 300 km s^{-1}. Our main conclusions are the following:

- Most bulges do present radial stellar population gradients. The outer parts of bulges harbor weaker metallic absorption lines than the inner regions. The distribution of these gradients among bulges are generally well peaked. They also display a real intrinsic dispersion, implying the presence of a variety of star formation histories within a common framework.
- In a number of cases, the gradients in Mg_1 and Mg_2 do not follow those in Mgb. We suggest that this is due to the inclusion of carbon, traced by the C4668′ index, in their bands. This explains a number of apparent previous discrepancies between works dealing either with Mg_2 or Mgb, in particular for elliptical galaxies.
- We argue that the existence of a *correlation* between gradients and central velocity dispersion among bulges is not an appropriate terminology. Instead, one sees that bulges with large velocity dispersion can exhibit strong gradients (they can also have negligible ones), while this probability diminishes at lower σ. Below 125 km s^{-1}, we do not find any bulge with significant radial spectral gradient. The same kind of dual regime with the velocity dispersion was observed in elliptical galaxies. This gradual build-up of the index vs. σ relation can only be clearly observed for indices with large dynamical ranges.
- The Hubble type of the parent galaxy appears to be a secondary parameter, earlier types having statistically larger velocity dispersions than later ones. The strength of the gradients depends only weakly on the bulge effective radius. The difference in sensitivity to the effective radius on one hand, and to the velocity dispersion on the other hand, suggests that the depth of the gravitational potential in which bulges are embedded is the main property tracing the spatial distribution of their stellar population.
- Strong gradients are found in bulges with the most metal-rich central regions, while bulges with strong *and weak* gradients have comparable properties at the bulge effective radius. This indicates that the external regions of the bulges, which are typically the oldest and most metal-poor and therefore the first to form, share some universal properties. This also argues in favor of an outside-in scenario for the formation and evolution of bulges.
- The analysis using SSP models indicates that radial variations in luminosity-weighted mean metallicity are twice to three time larger (in logarithmic scale) than the variations in age. While [Fe/H] at the bulge effective radii are on average 0.4 dex (σ = 0.3 dex) lower than in the bulge central regions, the age difference is of the order of 1.5 Gyr (σ = 1.3 Gyr), the inner regions being younger. We have found only two galaxies with convincing signs of an "inverted" age gradient. The changes in [α/Fe] are small (of the order 0.1 dex) and rather constant among bulges.

As to the fundamental question of the influence of the disk on the bulge evolution, we make the following comments: In terms of stellar population properties, we do not find any obvious differences between ellipticals and bulges. On the contrary, it seems that our observations strengthen their resemblance. One requirement to properly compare the two families of spheroids is to match systems of similar velocity dispersion. The imprint of the disk influence is generally seen via the presence of a bar in spiral galaxies. Bournaud et al. (2005) determined that a cycle of bar formation and dissolution takes about 2 Gyr for Sb-Sc galaxies with masses and radii comparable to that of the Milky Way. Gas accretion allows the bar to reappear (Bournaud & Combes 2002). In terms of time scales, a scenario where bulges would be formed through secular evolution could thus be conceivable for late-type galaxies. However, for the time being, our study introduces two severe constraints to this type of scenario: (i) The action of the bar must preserve the observed gradients and star formation time scales (as measured by [α/Fe], whose measured values are significantly larger than those of disk stars); (ii) The age gradients produced by the bar cycles (formation to dissolution) must be consistent with those measured (peaked at ~1.5 Gyr). For example, if 2 to 3 bar cycles are necessary to build the bulge of an early-type galaxy from disk material, the bulge assembly timescale is larger than the one implied by the observed gradients.

We note that these remarks also hold for models where bulges grow by accretion of satellites, combined with the accretion of disk material (e.g., Eliche-Moral et al. 2006). Nevertheless, bars are ubiquitous among spirals, and their presence and action could explain part of the dispersion seen among the bulge properties at fixed velocity dispersion, in particular by wiping out strong gradients (see, e.g. Friedli et al. 1994). Contrary to what was found by Moorthy & Holtzman (2006), we do not find that younger ages in the centres of bulges are restricted to barred and/or boxy/peanuts shape galaxies. In fact, we do not find any difference between the stellar properties of barred and non-barred galaxies in our sample, as seen along their bulge minor axis.

Kobayashi (2004) has proposed, as a result of her simulations of elliptical galaxies, that galaxies with strong gradients originate from small and rapid mergers mimicking an initial (monolithic) collapse, whereas galaxies with weak gradients would reveal a sequence of more significant mergers (i.e., with small mass ratios). In a scenario where bulges and ellipticals form in a similar way, i.e., disks settling after the bulk of the stellar population in bulges is in place, this hypothesis would also fit part of the observations presented here. However, bulges with low velocity dispersions would then require a different formation mechanism.

Acknowledgements. This work was supported by the Spanish research project AYA 2003-01840

References

Allen, P. D., Driver, S. P., Graham, A. W., et al. 2006, MNRAS, 371, 2
Barnes, J., & White, S. D. M. 1984, MNRAS, 211, 753
Bica, E. 1988, A&A, 195, 76
Bournaud, F., & Combes, F. 2002, A&A, 392, 83
Bournaud, F., Combes, F., & Semelin, B. 2005, MNRAS, 364, L18
Carollo, C. M., Danziger, I. J., & Buson, L. 1993, MNRAS, 265, 553
Chung, A., & Bureau, M. 2004, AJ, 127, 3192
de Jong, R. S. 1996, A&A, 313, 45
de Jong, R. S., Simard, L., Davies, R. L., et al. 2004, MNRAS, 355, 1155
Eliche-Moral, M. C., Balcells, M., Aguerri, J. A. L., & González-García, A. C. 2006, A&A, 457, 91
Falcón-Barroso, J., Peletier, R. F., & Balcells, M. 2002, MNRAS, 335, 741
Friedli, D., Benz, W., & Kennicutt, R. 1994, ApJ, 430, L105
Ganda, K., Falcón-Barroso, J., Peletier, R. F., et al. 2006, MNRAS, 367, 46
Gorgas, J., Jablonka, P., & Goudfrooij, P. 2007, A&A, 474, 1081
Gorgas, J., Pedraz, S., Guzman, R., Cardiel, N., & Gonzalez, J. J. 1997, ApJ, 481, L19
Goudfrooij, P., & Emsellem, E. 1996, A&A, 306, L45
Idiart, T. P., de Freitas Pacheco, J. A., & Costa, R. D. D. 1996, AJ, 112, 2541
Jablonka, P., Martin, P., & Arimoto, N. 1996, AJ, 112, 1415
Kobayashi, C. 2004, MNRAS, 347, 740
Lauberts, A. 1982, ESO/Uppsala survey of the ESO(B) atlas (Garching: European Southern Observatory (ESO))

Mehlert, D., Thomas, D., Saglia, R. P., Bender, R., & Wegner, G. 2003, A&A, 407, 423
Moorthy, B. K., & Holtzman, J. A. 2006, MNRAS, 371, 583
Nilson, P. 1973, Uppsala general catalogue of galaxies (Acta Universitatis Upsaliensis. Nova Acta Regiae Societatis Scientiarum Upsaliensis - Uppsala Astronomiska Observatoriums Annaler, Uppsala: Astronomiska Observatorium, 1973)
Ogando, R. L. C., Maia, M. A. G., Chiappini, C., et al. 2005, ApJ, 632, L61
Olsen, K. A. G., Blum, R. D., Stephens, A. W., et al. 2006, AJ, 132, 271
Proctor, R. N., & Sansom, A. E. 2002, MNRAS, 333, 517
Proctor, R. N., Sansom, A. E., & Reid, I. N. 2000, MNRAS, 311, 37
Saglia, R. P., Bertschinger, E., Baggley, G., et al. 1997, ApJS, 109, 79
Sánchez-Blázquez, P., Gorgas, J., & Cardiel, N. 2006, A&A, 457, 823
Sansom, A. E., Peace, G., & Dodd, M. 1994, MNRAS, 271, 39
Sarajedini, A., & Jablonka, P. 2005, AJ, 130, 1627
Sheth, K., Vogel, S. N., Regan, M. W., Thornley, M. D., & Teuben, P. J. 2005, ApJ, 632, 217
Simien, F., & de Vaucouleurs, G. 1986, ApJ, 302, 564
Thomas, D., & Davies, R. L. 2006, MNRAS, 366, 510
Thomas, D., Maraston, C., & Bender, R. 2003, MNRAS, 339, 897
Thomas, D., Maraston, C., & Korn, A. 2004, MNRAS, 351, L19
Vazdekis, A. 1999, ApJ, 513, 224
Worthey, G. 1994, ApJS, 95, 107
Worthey, G. 1998, PASP, 110, 888
Worthey, G., & Ottaviani, D. L. 1997, ApJS, 111, 377

Online Material

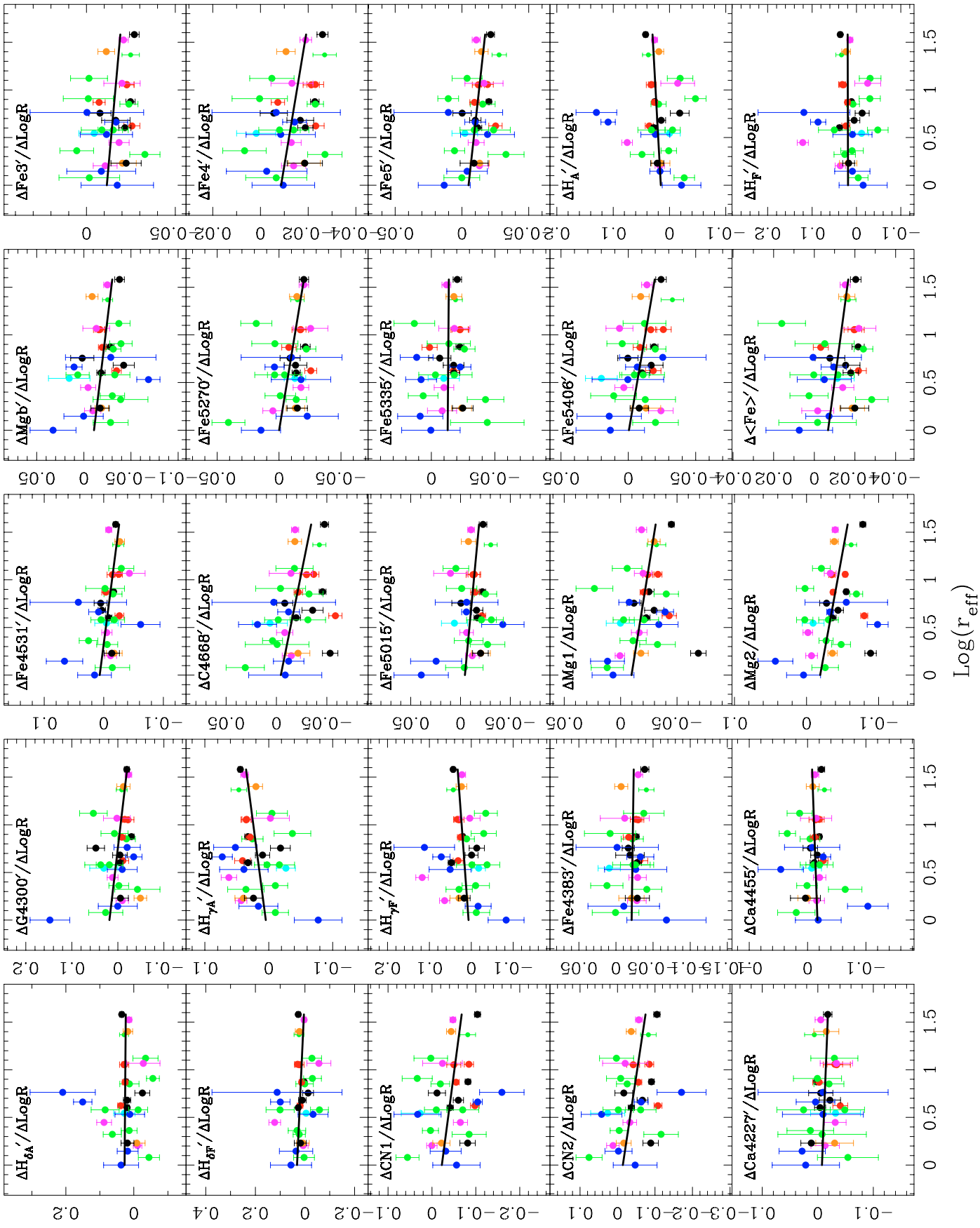

Fig. 6. The relation between the gradients and the bulge effective radii for the 25 indices that are available for the whole sample of bulges. The color code for the different Hubble types is the same as in Fig. 4.

Table 1. For each of our sample galaxy, the 33 measured gradients (first line) and their attached errors (second line) are presented.

NGC 522	$H\delta'_A$	$H\delta'_F$	CN1	CN2	Ca4227′	G-band	$H\gamma'_A$	$H\gamma'_F$	Fe4383′	Ca4455′	Fe4531′
	0.0280	−0.0048	0.0269	0.0261	−0.0322	0.0307	−0.0268	−0.0176	0.0091	−0.0071	−0.0046
	0.0312	0.0264	0.0430	0.0454	0.0451	0.0306	0.0149	0.0159	0.0150	0.0166	0.0196
	C4668′	Hβ′	Fe5015′	Mg1	Mg2	Mgb	Fe5270′	Fe5335′	Fe5406′	Fe5709′	Fe5782′
	0.0065	−0.1466	0.0061	0.0002	−0.0092	0.0155	−0.0128	−0.0097	0.0200	99.0000	99.0000
	0.0174	0.0890	0.0131	0.0125	0.0151	0.0220	0.0087	0.0123	0.0118	99.0000	99.0000
	Na5895′	TiO1	TiO2	<Fe>′	Fe3′	Fe4′	Fe5′	Fe6′	H'_A	H'_F	Balmer
	99.0000	99.0000	99.0000	−0.0113	−0.0043	0.0018	−0.0021	99.0000	−0.0001	−0.0117	−0.1290
	99.0000	99.0000	99.0000	0.0083	0.0086	0.0082	0.0096	99.0000	0.0191	0.0154	0.0699
NGC 585	$H\delta'_A$	$H\delta'_F$	CN1	CN2	Ca4227′	G-band	$H\gamma'_A$	$H\gamma'_F$	Fe4383′	Ca4455′	Fe4531′
	−0.0086	0.0083	−0.0216	−0.0165	−0.0304	−0.0488	0.0395	0.0292	−0.0208	−0.0001	−0.0176
	0.0245	0.0255	0.0197	0.0198	0.0340	0.0136	0.0135	0.0216	0.0170	0.0167	0.0132
	C4668′	Hβ′	Fe5015′	Mg1	Mg2	Mgb	Fe5270′	Fe5335′	Fe5406′	Fe5709′	Fe5782′
	−0.0215	−0.0459	−0.0205	−0.0180	−0.0360	−0.0189	−0.0132	−0.0238	−0.0131	−0.0101	−0.0087
	0.0116	0.0331	0.0094	0.0065	0.0064	0.0071	0.0075	0.0078	0.0109	0.0062	0.0130
	Na5895′	TiO1	TiO2	<Fe>′	Fe3′	Fe4′	Fe5′	Fe6′	H'_A	H'_F	Balmer
	−0.1275	−0.0013	0.0056	−0.0186	−0.0202	−0.0184	−0.0133	−0.0116	0.0155	0.0188	−0.0341
	0.0194	0.0045	0.0053	0.0061	0.0078	0.0067	0.0072	0.0053	0.0162	0.0195	0.0308
NGC 678	$H\delta'_A$	$H\delta'_F$	CN1	CN2	Ca4227′	G-band	$H\gamma'_A$	$H\gamma'_F$	Fe4383′	Ca4455′	Fe4531′
	0.0289	0.0241	−0.0817	−0.0823	0.0063	−0.0083	0.0468	0.0432	−0.0410	−0.0289	−0.0244
	0.0131	0.0197	0.0177	0.0208	0.0173	0.0117	0.0122	0.0153	0.0102	0.0112	0.0092
	C4668′	Hβ′	Fe5015′	Mg1	Mg2	Mgb	Fe5270′	Fe5335′	Fe5406′	Fe5709′	Fe5782′
	−0.0426	0.0111	−0.0303	−0.0317	−0.0618	−0.0252	−0.0149	−0.0189	−0.0327	99.0000	99.0000
	0.0065	0.0455	0.0065	0.0083	0.0075	0.0054	0.0054	0.0054	0.0084	99.0000	99.0000
	Na5895′	TiO1	TiO2	<Fe>′	Fe3′	Fe4′	Fe5′	Fe6′	H'_A	H'_F	Balmer
	99.0000	99.0000	99.0000	−0.0168	−0.0249	−0.0269	−0.0279	99.0000	0.0374	0.0339	0.0005
	99.0000	99.0000	99.0000	0.0037	0.0049	0.0049	0.0054	99.0000	0.0104	0.0125	0.0269
NGC 891	$H\delta'_A$	$H\delta'_F$	CN1	CN2	Ca4227′	G-band	$H\gamma'_A$	$H\gamma'_F$	Fe4383′	Ca4455′	Fe4531′
	−0.0342	−0.0281	0.0027	0.0026	−0.0299	0.0532	−0.0050	−0.0347	−0.0375	0.0137	−0.0295
	0.0371	0.0390	0.0382	0.0455	0.0423	0.0300	0.0242	0.0273	0.0272	0.0215	0.0210
	C4668′	Hβ′	Fe5015′	Mg1	Mg2	Mgb	Fe5270′	Fe5335′	Fe5406′	Fe5709′	Fe5782′
	−0.0179	−0.0550	0.0047	−0.0058	−0.0206	−0.0371	0.0184	0.0134	−0.0120	99.0000	99.0000
	0.0185	0.0297	0.0129	0.0131	0.0123	0.0119	0.0126	0.0160	0.0159	99.0000	99.0000
	Na5895′	TiO1	TiO2	<Fe>′	Fe3′	Fe4′	Fe5′	Fe6′	H'_A	H'_F	Balmer
	99.0000	99.0000	99.0000	0.0160	−0.0014	−0.0048	−0.0038	99.0000	−0.0188	−0.0309	−0.0115
	99.0000	99.0000	99.0000	0.0117	0.0104	0.0093	0.0112	99.0000	0.0226	0.0244	0.0428
NGC 973	$H\delta'_A$	$H\delta'_F$	CN1	CN2	Ca4227′	G-band	$H\gamma'_A$	$H\gamma'_F$	Fe4383′	Ca4455′	Fe4531′
	0.0120	−0.0326	0.0328	0.0425	−0.0092	−0.0095	0.0390	0.0507	−0.0266	0.0461	−0.0617
	0.0435	0.0604	0.0536	0.0543	0.0728	0.0323	0.0380	0.0501	0.0419	0.0389	0.0328
	C4668′	Hβ′	Fe5015′	Mg1	Mg2	Mgb	Fe5270′	Fe5335′	Fe5406′	Fe5709′	Fe5782′
	0.0188	0.0425	−0.0425	−0.0338	−0.0986	−0.0685	−0.0178	0.0081	0.0003	99.0000	99.0000
	0.0189	0.0629	0.0213	0.0171	0.0144	0.0123	0.0240	0.0121	0.0266	99.0000	99.0000
	Na5895′	TiO1	TiO2	<Fe>′	Fe3′	Fe4′	Fe5′	Fe6′	H'_A	H'_F	Balmer
	99.0000	99.0000	99.0000	−0.0049	−0.0112	−0.0085	−0.0191	99.0000	0.0251	0.0091	0.0537
	99.0000	99.0000	99.0000	0.0133	0.0147	0.0145	0.0202	99.0000	0.0257	0.0442	0.0348
NGC 1032	$H\delta'_A$	$H\delta'_F$	CN1	CN2	Ca4227′	G-band	$H\gamma'_A$	$H\gamma'_F$	Fe4383′	Ca4455′	Fe4531′
	0.0273	0.0296	−0.0841	−0.0847	−0.0307	−0.0147	0.0346	0.0331	−0.0271	−0.0201	−0.0252
	0.0070	0.0123	0.0105	0.0117	0.0140	0.0091	0.0073	0.0092	0.0078	0.0084	0.0062
	C4668′	Hβ′	Fe5015′	Mg1	Mg2	Mgb	Fe5270′	Fe5335′	Fe5406′	Fe5709′	Fe5782′
	−0.0370	0.0099	−0.0139	−0.0331	−0.0536	−0.0171	−0.0175	−0.0226	−0.0260	99.0000	99.0000
	0.0052	0.0123	0.0063	0.0036	0.0027	0.0052	0.0043	0.0063	0.0058	99.0000	99.0000
	Na5895′	TiO1	TiO2	<Fe>′	Fe3′	Fe4′	Fe5′	Fe6′	H'_A	H'_F	Balmer
	99.0000	99.0000	99.0000	−0.0200	−0.0227	−0.0230	−0.0191	99.0000	0.0323	0.0323	0.0333
	99.0000	99.0000	99.0000	0.0034	0.0041	0.0035	0.0044	99.0000	0.0051	0.0080	0.0095
NGC 1184	$H\delta'_A$	$H\delta'_F$	CN1	CN2	Ca4227′	G-band	$H\gamma'_A$	$H\gamma'_F$	Fe4383′	Ca4455′	Fe4531′
	0.0286	0.0224	−0.0498	−0.0418	−0.0343	−0.0221	0.0355	0.0294	−0.0298	−0.0137	−0.0143
	0.0134	0.0187	0.0159	0.0171	0.0244	0.0127	0.0079	0.0120	0.0077	0.0112	0.0087
	C4668′	Hβ′	Fe5015′	Mg1	Mg2	Mgb	Fe5270′	Fe5335′	Fe5406′	Fe5709′	Fe5782′
	−0.0300	−0.0046	−0.0125	−0.0240	−0.0351	−0.0160	−0.0171	−0.0224	−0.0167	99.0000	99.0000
	0.0069	0.0147	0.0069	0.0043	0.0044	0.0058	0.0067	0.0070	0.0044	99.0000	99.0000
	Na5895′	TiO1	TiO2	<Fe>′	Fe3′	Fe4′	Fe5′	Fe6′	H'_A	H'_F	Balmer
	99.0000	99.0000	99.0000	−0.0196	−0.0227	−0.0213	−0.0123	99.0000	0.0324	0.0294	0.0263
	99.0000	99.0000	99.0000	0.0050	0.0041	0.0034	0.0045	99.0000	0.0087	0.0098	0.0173

NGC 1351A	$H\delta'_A$	$H\delta'_F$	CN1	CN2	Ca4227′	G-band	$H\gamma'_A$	$H\gamma'_F$	Fe4383′	Ca4455′	Fe4531′
	0.2095	0.1126	−0.1592	−0.1708	−0.0095	−0.0201	0.0523	0.1123	−0.0016	−0.0078	0.0428
	0.0960	0.2621	0.0506	0.0653	0.1171	0.0285	0.0339	0.0723	0.0554	0.0474	0.0810
	C4668′	Hβ′	Fe5015′	Mg1	Mg2	Mgb	Fe5270′	Fe5335′	Fe5406′	Fe5709′	Fe5782′
	0.0027	0.0276	−0.0061	−0.0076	−0.0551	−0.0285	−0.0101	0.0116	−0.0256	0.0026	0.0029
	0.0613	0.1094	0.0315	0.0092	0.0572	0.0480	0.0408	0.0129	0.0321	0.0249	0.0329
	Na5895′	TiO1	TiO2	<Fe>′	Fe3′	Fe4′	Fe5′	Fe6′	H'_A	H'_F	Balmer
	−0.0365	−0.0242	0.0108	0.0006	−0.0002	−0.0066	0.0102	0.0070	0.1298	0.1183	0.1698
	0.0560	0.0178	0.0153	0.0238	0.0320	0.0269	0.0407	0.0339	0.0362	0.1035	0.1063
NGC 1886	$H\delta'_A$	$H\delta'_F$	CN1	CN2	Ca4227′	G-band	$H\gamma'_A$	$H\gamma'_F$	Fe4383′	Ca4455′	Fe4531′
	−0.0109	0.0071	0.0002	0.0122	−0.0133	−0.0096	0.0433	0.0638	−0.0281	−0.0156	−0.0115
	0.0127	0.0196	0.0118	0.0167	0.0255	0.0135	0.0091	0.0123	0.0126	0.0132	0.0100
	C4668′	Hβ′	Fe5015′	Mg1	Mg2	Mgb	Fe5270′	Fe5335′	Fe5406′	Fe5709′	Fe5782′
	−0.0147	99.0000	−0.0119	0.0006	−0.0070	−0.0094	0.0051	−0.0084	−0.0242	99.0000	99.0000
	0.0090	99.0000	0.0068	0.0042	0.0081	0.0087	0.0080	0.0115	0.0091	99.0000	99.0000
	Na5895′	TiO1	TiO2	<Fe>′	Fe3′	Fe4′	Fe5′	Fe6′	H'_A	H'_F	Balmer
	99.0000	99.0000	99.0000	−0.0017	−0.0105	−0.0139	−0.0131	99.0000	0.0174	0.0365	99.0000
	99.0000	99.0000	99.0000	0.0079	0.0067	0.0051	0.0068	99.0000	0.0081	0.0115	99.0000
NGC 3957	$H\delta'_A$	$H\delta'_F$	CN1	CN2	Ca4227′	G-band	$H\gamma'_A$	$H\gamma'_F$	Fe4383′	Ca4455′	Fe4531′
	0.0196	0.0270	−0.0414	−0.0369	−0.0042	−0.0044	0.0327	0.0476	−0.0282	−0.0115	−0.0082
	0.0059	0.0071	0.0070	0.0085	0.0099	0.0071	0.0059	0.0076	0.0061	0.0071	0.0054
	C4668′	Hβ′	Fe5015′	Mg1	Mg2	Mgb	Fe5270′	Fe5335′	Fe5406′	Fe5709′	Fe5782′
	−0.0196	−0.0266	−0.0170	−0.0228	−0.0360	−0.0182	−0.0138	−0.0177	−0.0102	99.0000	99.0000
	0.0043	0.0159	0.0035	0.0033	0.0049	0.0044	0.0033	0.0046	0.0059	99.0000	99.0000
	Na5895′	TiO1	TiO2	<Fe>′	Fe3′	Fe4′	Fe5′	Fe6′	H'_A	H'_F	Balmer
	99.0000	99.0000	99.0000	−0.0180	−0.0216	−0.0188	−0.0118	99.0000	0.0279	0.0382	0.0086
	99.0000	99.0000	99.0000	0.0038	0.0034	0.0032	0.0030	99.0000	0.0045	0.0053	0.0135
NGC 5084	$H\delta'_A$	$H\delta'_F$	CN1	CN2	Ca4227′	G-band	$H\gamma'_A$	$H\gamma'_F$	Fe4383′	Ca4455′	Fe4531′
	0.0358	0.0265	−0.1038	−0.1053	−0.0180	−0.0194	0.0445	0.0431	−0.0388	−0.0236	−0.0200
	0.0057	0.0074	0.0068	0.0083	0.0075	0.0054	0.0033	0.0037	0.0055	0.0058	0.0042
	C4668′	Hβ′	Fe5015′	Mg1	Mg2	Mgb	Fe5270′	Fe5335′	Fe5406′	Fe5709′	Fe5782′
	−0.0477	−0.0562	−0.0226	−0.0450	−0.0780	−0.0379	−0.0201	−0.0204	−0.0243	99.0000	99.0000
	0.0040	0.0558	0.0038	0.0025	0.0039	0.0051	0.0037	0.0033	0.0039	99.0000	99.0000
	Na5895′	TiO1	TiO2	<Fe>′	Fe3′	Fe4′	Fe5′	Fe6′	H'_A	H'_F	Balmer
	99.0000	99.0000	99.0000	−0.0204	−0.0269	−0.0260	−0.0214	99.0000	0.0423	0.0365	−0.0004
	99.0000	99.0000	99.0000	0.0026	0.0027	0.0023	0.0030	99.0000	0.0035	0.0040	0.0572
NGC 6010	$H\delta'_A$	$H\delta'_F$	CN1	CN2	Ca4227′	G-band	$H\gamma'_A$	$H\gamma'_F$	Fe4383′	Ca4455′	Fe4531′
	0.0386	0.0200	−0.0978	−0.1080	−0.0405	−0.0109	0.0410	0.0315	−0.0319	−0.0268	−0.0263
	0.0090	0.0114	0.0099	0.0106	0.0134	0.0123	0.0124	0.0119	0.0108	0.0081	0.0073
	C4668′	Hβ′	Fe5015′	Mg1	Mg2	Mgb	Fe5270′	Fe5335′	Fe5406′	Fe5709′	Fe5782′
	−0.0585	99.0000	−0.0215	−0.0431	−0.0800	−0.0347	−0.0256	−0.0174	−0.0185	99.0000	99.0000
	0.0066	99.0000	0.0037	0.0063	0.0049	0.0049	0.0048	0.0045	0.0057	99.0000	99.0000
	Na5895′	TiO1	TiO2	<Fe>′	Fe3′	Fe4′	Fe5′	Fe6′	H'_A	H'_F	Balmer
	99.0000	99.0000	99.0000	−0.0217	−0.0256	−0.0232	−0.0251	99.0000	0.0359	0.0239	99.0000
	99.0000	99.0000	99.0000	0.0039	0.0045	0.0035	0.0050	99.0000	0.0071	0.0091	99.0000
NGC 6829	$H\delta'_A$	$H\delta'_F$	CN1	CN2	Ca4227′	G-band	$H\gamma'_A$	$H\gamma'_F$	Fe4383′	Ca4455′	Fe4531′
	0.0130	0.0013	−0.0190	−0.0256	−0.0201	−0.0188	0.0255	0.0111	−0.0219	−0.0042	−0.0155
	0.0282	0.0353	0.0212	0.0284	0.0270	0.0190	0.0166	0.0185	0.0149	0.0170	0.0152
	C4668′	Hβ′	Fe5015′	Mg1	Mg2	Mgb	Fe5270′	Fe5335′	Fe5406′	Fe5709′	Fe5782′
	−0.0323	−0.0376	−0.0251	−0.0405	−0.0690	−0.0313	−0.0220	−0.0260	−0.0200	99.0000	99.0000
	0.0140	0.0481	0.0112	0.0108	0.0089	0.0080	0.0077	0.0083	0.0079	99.0000	99.0000
	Na5895′	TiO1	TiO2	<Fe>′	Fe3′	Fe4′	Fe5′	Fe6′	H'_A	H'_F	Balmer
	99.0000	99.0000	99.0000	−0.0242	−0.0239	−0.0230	−0.0155	99.0000	0.0194	0.0079	0.0705
	99.0000	99.0000	99.0000	0.0046	0.0051	0.0034	0.0093	99.0000	0.0134	0.0147	0.0522
NGC 7183	$H\delta'_A$	$H\delta'_F$	CN1	CN2	Ca4227′	G-band	$H\gamma'_A$	$H\gamma'_F$	Fe4383′	Ca4455′	Fe4531′
	0.0542	0.0644	−0.0671	−0.0555	−0.0219	−0.0048	0.0155	0.0167	−0.0112	0.0075	0.0005
	0.0101	0.0144	0.0106	0.0124	0.0136	0.0075	0.0071	0.0091	0.0102	0.0084	0.0059
	C4668′	Hβ′	Fe5015′	Mg1	Mg2	Mgb	Fe5270′	Fe5335′	Fe5406′	Fe5709′	Fe5782′
	−0.0209	−0.0844	−0.0124	−0.0263	−0.0330	−0.0067	−0.0102	−0.0064	−0.0128	−0.0147	−0.0128
	0.0042	0.0762	0.0039	0.0036	0.0031	0.0046	0.0061	0.0043	0.0054	0.0049	0.0056
	Na5895′	TiO1	TiO2	<Fe>′	Fe3′	Fe4′	Fe5′	Fe6′	H'_A	H'_F	Balmer
	−0.1002	−0.0120	−0.0115	−0.0084	−0.0092	−0.0102	−0.0014	−0.0067	0.0340	0.0400	−0.1497
	0.0060	0.0038	0.0031	0.0040	0.0042	0.0034	0.0043	0.0023	0.0075	0.0097	0.0748
NGC 7264	$H\delta'_A$	$H\delta'_F$	CN1	CN2	Ca4227′	G-band	$H\gamma'_A$	$H\gamma'_F$	Fe4383′	Ca4455′	Fe4531′
	−0.0442	0.0039	0.0557	0.0759	−0.0543	0.0264	−0.0102	−0.0120	0.0005	0.0193	−0.0145
	0.0310	0.0418	0.0262	0.0347	0.0548	0.0371	0.0207	0.0319	0.0314	0.0320	0.0289
	C4668′	Hβ′	Fe5015′	Mg1	Mg2	Mgb	Fe5270′	Fe5335′	Fe5406′	Fe5709′	Fe5782′
	0.0310	99.0000	−0.0038	0.0118	−0.0258	−0.0284	0.0409	−0.0440	−0.0202	99.0000	99.0000
	0.0190	99.0000	0.0188	0.0143	0.0184	0.0185	0.0133	0.0289	0.0169	99.0000	99.0000
	Na5895′	TiO1	TiO2	<Fe>′	Fe3′	Fe4′	Fe5′	Fe6′	H'_A	H'_F	Balmer
	99.0000	99.0000	99.0000	−0.0016	−0.0016	−0.0066	0.0001	99.0000	−0.0263	−0.0041	99.0000
	99.0000	99.0000	99.0000	0.0191	0.0171	0.0128	0.0134	99.0000	0.0182	0.0219	99.0000

NGC 7332	$H\delta'_A$	$H\delta'_F$	CN1	CN2	Ca4227′	G-band	$H\gamma'_A$	$H\gamma'_F$	Fe4383′	Ca4455′	Fe4531′
	0.0231	0.0032	−0.0819	−0.0907	0.0022	−0.0291	0.0326	0.0202	−0.0271	−0.0203	−0.0166
	0.0061	0.0055	0.0062	0.0071	0.0048	0.0061	0.0049	0.0046	0.0039	0.0040	0.0027
	C4668′	Hβ′	Fe5015′	Mg1	Mg2	Mgb	Fe5270′	Fe5335′	Fe5406′	Fe5709′	Fe5782′
	−0.0458	99.0000	−0.0220	−0.0251	−0.0550	−0.0280	−0.0212	−0.0224	−0.0192	99.0000	99.0000
	0.0034	99.0000	0.0033	0.0046	0.0029	0.0039	0.0039	0.0031	0.0028	99.0000	99.0000
	Na5895′	TiO1	TiO2	<Fe>′	Fe3′	Fe4′	Fe5′	Fe6′	H'_A	H'_F	Balmer
	99.0000	99.0000	99.0000	−0.0216	−0.0248	−0.0228	−0.0201	99.0000	0.0263	0.0115	99.0000
	99.0000	99.0000	99.0000	0.0030	0.0026	0.0018	0.0020	99.0000	0.0030	0.0033	99.0000
NGC 7396	$H\delta'_A$	$H\delta'_F$	CN1	CN2	Ca4227′	G-band	$H\gamma'_A$	$H\gamma'_F$	Fe4383′	Ca4455′	Fe4531′
	0.0176	0.0222	−0.0437	−0.0364	−0.0154	−0.0120	0.0200	0.0236	−0.0070	−0.0088	−0.0267
	0.0139	0.0165	0.0106	0.0128	0.0226	0.0144	0.0102	0.0127	0.0088	0.0111	0.0081
	C4668′	Hβ′	Fe5015′	Mg1	Mg2	Mgb	Fe5270′	Fe5335′	Fe5406′	Fe5709′	Fe5782′
	−0.0182	−0.0557	−0.0080	−0.0297	−0.0385	−0.0087	−0.0144	−0.0177	−0.0092	99.0000	99.0000
	0.0067	0.0376	0.0072	0.0054	0.0055	0.0063	0.0060	0.0062	0.0063	99.0000	99.0000
	Na5895′	TiO1	TiO2	<Fe>′	Fe3′	Fe4′	Fe5′	Fe6′	H'_A	H'_F	Balmer
	99.0000	99.0000	99.0000	−0.0160	−0.0111	−0.0107	−0.0146	99.0000	0.0190	0.0233	−0.0676
	99.0000	99.0000	99.0000	0.0040	0.0047	0.0039	0.0050	99.0000	0.0087	0.0097	0.0452
NGC 7703	$H\delta'_A$	$H\delta'_F$	CN1	CN2	Ca4227′	G-band	$H\gamma'_A$	$H\gamma'_F$	Fe4383′	Ca4455′	Fe4531′
	0.0199	0.0104	−0.0602	−0.0665	−0.0219	−0.0044	0.0097	−0.0006	−0.0189	−0.0168	0.0032
	0.0106	0.0152	0.0116	0.0143	0.0192	0.0158	0.0112	0.0155	0.0192	0.0114	0.0062
	C4668′	Hβ′	Fe5015′	Mg1	Mg2	Mgb	Fe5270′	Fe5335′	Fe5406′	Fe5709′	Fe5782′
	−0.0358	0.1954	−0.0160	−0.0298	−0.0437	−0.0423	−0.0133	−0.0175	−0.0170	99.0000	99.0000
	0.0105	0.0810	0.0064	0.0085	0.0073	0.0112	0.0092	0.0081	0.0088	99.0000	99.0000
	Na5895′	TiO1	TiO2	<Fe>′	Fe3′	Fe4′	Fe5′	Fe6′	H'_A	H'_F	Balmer
	99.0000	99.0000	99.0000	−0.0154	−0.0165	−0.0167	−0.0100	99.0000	0.0147	0.0049	0.0324
	99.0000	99.0000	99.0000	0.0071	0.0080	0.0056	0.0043	99.0000	0.0079	0.0124	0.0428
NGC 7814	$H\delta'_A$	$H\delta'_F$	CN1	CN2	Ca4227′	G-band	$H\gamma'_A$	$H\gamma'_F$	Fe4383′	Ca4455′	Fe4531′
	0.0144	0.0037	−0.0476	−0.0572	−0.0055	−0.0229	0.0378	0.0225	−0.0299	−0.0127	−0.0084
	0.0083	0.0096	0.0065	0.0092	0.0104	0.0071	0.0060	0.0087	0.0060	0.0065	0.0050
	C4668′	Hβ′	Fe5015′	Mg1	Mg2	Mgb	Fe5270′	Fe5335′	Fe5406′	Fe5709′	Fe5782′
	−0.0185	0.0008	−0.0106	−0.0185	−0.0397	−0.0249	−0.0200	−0.0118	−0.0138	99.0000	99.0000
	0.0036	0.0054	0.0033	0.0046	0.0041	0.0038	0.0038	0.0035	0.0039	99.0000	99.0000
	Na5895′	TiO1	TiO2	<Fe>′	Fe3′	Fe4′	Fe5′	Fe6′	H'_A	H'_F	Balmer
	99.0000	99.0000	99.0000	−0.0152	−0.0209	−0.0190	−0.0107	99.0000	0.0265	0.0149	0.0219
	99.0000	99.0000	99.0000	0.0025	0.0026	0.0024	0.0030	99.0000	0.0050	0.0066	0.0044
IC 1711	$H\delta'_A$	$H\delta'_F$	CN1	CN2	Ca4227′	G-band	$H\gamma'_A$	$H\gamma'_F$	Fe4383′	Ca4455′	Fe4531′
	0.0634	0.0232	−0.0847	−0.1163	−0.0078	−0.0424	0.0358	0.0291	−0.0415	−0.0645	−0.0059
	0.0267	0.0245	0.0389	0.0460	0.0796	0.0491	0.0285	0.0315	0.0201	0.0287	0.0176
	C4668′	Hβ′	Fe5015′	Mg1	Mg2	Mgb	Fe5270′	Fe5335′	Fe5406′	Fe5709′	Fe5782′
	−0.0007	99.0000	−0.0271	−0.0327	−0.0479	−0.0389	−0.0139	−0.0426	−0.0126	99.0000	99.0000
	0.0316	99.0000	0.0174	0.0158	0.0130	0.0291	0.0083	0.0144	0.0224	99.0000	99.0000
	Na5895′	TiO1	TiO2	<Fe>′	Fe3′	Fe4′	Fe5′	Fe6′	H'_A	H'_F	Balmer
	99.0000	99.0000	99.0000	−0.0283	−0.0329	−0.0270	−0.0330	99.0000	0.0488	0.0265	99.0000
	99.0000	99.0000	99.0000	0.0080	0.0085	0.0072	0.0135	99.0000	0.0210	0.0240	99.0000
IC 1970	$H\delta'_A$	$H\delta'_F$	CN1	CN2	Ca4227′	G-band	$H\gamma'_A$	$H\gamma'_F$	Fe4383′	Ca4455′	Fe4531′
	−0.0561	−0.0305	0.0335	−0.0082	0.0005	0.0074	−0.0370	−0.0297	0.0079	0.0347	−0.0022
	0.0188	0.0356	0.0342	0.0374	0.0434	0.0293	0.0287	0.0300	0.0345	0.0141	0.0325
	C4668′	Hβ′	Fe5015′	Mg1	Mg2	Mgb	Fe5270′	Fe5335′	Fe5406′	Fe5709′	Fe5782′
	−0.0041	99.0000	−0.0011	0.0232	0.0021	−0.0393	0.0034	−0.0137	0.0044	−0.0006	−0.0201
	0.0248	99.0000	0.0153	0.0163	0.0119	0.0119	0.0187	0.0170	0.0115	0.0137	0.0148
	Na5895′	TiO1	TiO2	<Fe>′	Fe3′	Fe4′	Fe5′	Fe6′	H'_A	H'_F	Balmer
	−0.0309	0.0181	−0.0038	−0.0051	−0.0010	0.0003	0.0103	0.0020	−0.0461	−0.0299	99.0000
	0.0143	0.0068	0.0117	0.0146	0.0141	0.0116	0.0078	0.0090	0.0188	0.0238	99.0000
IC 2531	$H\delta'_A$	$H\delta'_F$	CN1	CN2	Ca4227′	G-band	$H\gamma'_A$	$H\gamma'_F$	Fe4383′	Ca4455′	Fe4531′
	0.0139	0.0322	0.0034	−0.0047	0.0134	−0.0019	−0.0101	−0.0105	0.0123	0.0010	0.0256
	0.0233	0.0351	0.0183	0.0244	0.0421	0.0213	0.0195	0.0327	0.0218	0.0177	0.0156
	C4668′	Hβ′	Fe5015′	Mg1	Mg2	Mgb	Fe5270′	Fe5335′	Fe5406′	Fe5709′	Fe5782′
	0.0039	−0.0133	−0.0082	−0.0111	−0.0271	−0.0303	−0.0010	0.0065	0.0109	99.0000	99.0000
	0.0099	0.0230	0.0145	0.0116	0.0098	0.0129	0.0124	0.0117	0.0170	99.0000	99.0000
	Na5895′	TiO1	TiO2	<Fe>′	Fe3′	Fe4′	Fe5′	Fe6′	H'_A	H'_F	Balmer
	99.0000	99.0000	99.0000	0.0026	0.0055	0.0067	0.0056	99.0000	0.0013	0.0100	−0.0036
	99.0000	99.0000	99.0000	0.0094	0.0095	0.0091	0.0076	99.0000	0.0137	0.0253	0.0141
IC 5176	$H\delta'_A$	$H\delta'_F$	CN1	CN2	Ca4227′	G-band	$H\gamma'_A$	$H\gamma'_F$	Fe4383′	Ca4455′	Fe4531′
	0.1505	0.0995	−0.1042	−0.0630	0.0041	−0.0344	0.0729	0.0715	−0.0328	−0.0267	0.0087
	0.0270	0.0392	0.0106	0.0185	0.0347	0.0178	0.0159	0.0206	0.0181	0.0129	0.0166
	C4668′	Hβ′	Fe5015′	Mg1	Mg2	Mgb	Fe5270′	Fe5335′	Fe5406′	Fe5709′	Fe5782′
	−0.0120	99.0000	−0.0060	−0.0394	−0.0326	0.0104	0.0037	−0.0227	−0.0067	−0.0083	−0.0123
	0.0108	99.0000	0.0049	0.0075	0.0046	0.0085	0.0077	0.0084	0.0087	0.0071	0.0078
	Na5895′	TiO1	TiO2	<Fe>′	Fe3′	Fe4′	Fe5′	Fe6′	H'_A	H'_F	Balmer
	−0.0608	−0.0042	−0.0123	−0.0095	−0.0167	−0.0143	−0.0099	−0.0100	0.1090	0.0864	99.0000
	0.0118	0.0072	0.0044	0.0062	0.0065	0.0050	0.0078	0.0057	0.0127	0.0171	99.0000

IC 5264	$H\delta'_A$	$H\delta'_F$	CN1	CN2	Ca4227′	G-band	$H\gamma'_A$	$H\gamma'_F$	Fe4383′	Ca4455′	Fe4531′
	0.0875	0.1218	−0.0649	−0.0328	−0.0315	0.0116	0.0624	0.1176	−0.0291	−0.0207	−0.0052
	0.0217	0.0234	0.0160	0.0181	0.0196	0.0117	0.0120	0.0151	0.0117	0.0106	0.0086
	C4668′	Hβ′	Fe5015′	Mg1	Mg2	Mgb	Fe5270′	Fe5335′	Fe5406′	Fe5709′	Fe5782′
	−0.0082	0.1346	−0.0061	−0.0165	−0.0017	−0.0046	−0.0177	−0.0099	0.0033	0.0018	−0.0081
	0.0081	0.1174	0.0068	0.0070	0.0066	0.0080	0.0063	0.0077	0.0067	0.0059	0.0081
	Na5895′	TiO1	TiO2	<Fe>′	Fe3′	Fe4′	Fe5′	Fe6′	H'_A	H'_F	Balmer
	−0.0501	−0.0012	−0.0008	−0.0140	−0.0183	−0.0129	−0.0106	−0.0076	0.0753	0.1210	0.1254
	0.0113	0.0042	0.0043	0.0055	0.0057	0.0042	0.0060	0.0048	0.0095	0.0126	0.1186
UGC 10043	$H\delta'_A$	$H\delta'_F$	CN1	CN2	Ca4227′	G-band	$H\gamma'_A$	$H\gamma'_F$	Fe4383′	Ca4455′	Fe4531′
	0.0377	0.0563	−0.0558	−0.0471	0.0215	0.1476	−0.0773	−0.0831	−0.0680	−0.0183	0.0155
	0.0515	0.0829	0.0538	0.0583	0.0606	0.0432	0.0374	0.0428	0.0533	0.0393	0.0282
	C4668′	Hβ′	Fe5015′	Mg1	Mg2	Mgb	Fe5270′	Fe5335′	Fe5406′	Fe5709′	Fe5782′
	−0.0087	99.0000	0.0395	0.0067	0.0042	0.0327	0.0146	0.0004	0.0134	99.0000	99.0000
	0.0363	99.0000	0.0273	0.0185	0.0236	0.0244	0.0158	0.0230	0.0254	99.0000	99.0000
	Na5895′	TiO1	TiO2	<Fe>′	Fe3′	Fe4′	Fe5′	Fe6′	H'_A	H'_F	Balmer
	99.0000	99.0000	99.0000	0.0074	−0.0173	−0.0096	0.0133	99.0000	−0.0215	−0.0150	99.0000
	99.0000	99.0000	99.0000	0.0164	0.0204	0.0131	0.0195	99.0000	0.0343	0.0541	99.0000
UGC 11552	$H\delta'_A$	$H\delta'_F$	CN1	CN2	Ca4227′	G-band	$H\gamma'_A$	$H\gamma'_F$	Fe4383′	Ca4455′	Fe4531′
	−0.0280	−0.0561	−0.0240	−0.0206	−0.0335	0.0021	−0.0025	0.0036	−0.0119	−0.0146	−0.0430
	0.0490	0.0483	0.0453	0.0602	0.0291	0.0291	0.0297	0.0247	0.0330	0.0268	0.0265
	C4668′	Hβ′	Fe5015′	Mg1	Mg2	Mgb	Fe5270′	Fe5335′	Fe5406′	Fe5709′	Fe5782′
	−0.0144	0.0156	0.0102	−0.0199	−0.0329	−0.0132	−0.0255	−0.0181	0.0066	−0.0111	−0.0172
	0.0215	0.0658	0.0168	0.0077	0.0083	0.0142	0.0140	0.0123	0.0100	0.0086	0.0166
	Na5895′	TiO1	TiO2	<Fe>′	Fe3′	Fe4′	Fe5′	Fe6′	H'_A	H'_F	Balmer
	−0.0720	−0.0065	−0.0084	−0.0219	−0.0200	−0.0132	−0.0165	−0.0159	−0.0145	−0.0254	0.0046
	0.0131	0.0065	0.0100	0.0084	0.0102	0.0088	0.0143	0.0112	0.0299	0.0293	0.0664
UGC 11587	$H\delta'_A$	$H\delta'_F$	CN1	CN2	Ca4227′	G-band	$H\gamma'_A$	$H\gamma'_F$	Fe4383′	Ca4455′	Fe4531′
	−0.0249	−0.0127	−0.0112	−0.0168	−0.0054	0.0480	−0.0182	−0.0130	−0.0165	−0.0047	0.0052
	0.0219	0.0216	0.0195	0.0238	0.0218	0.0188	0.0156	0.0182	0.0082	0.0125	0.0109
	C4668′	Hβ′	Fe5015′	Mg1	Mg2	Mgb	Fe5270′	Fe5335′	Fe5406′	Fe5709′	Fe5782′
	−0.0082	0.0356	−0.0004	−0.0119	−0.0277	0.0017	−0.0089	−0.0066	0.0003	99.0000	99.0000
	0.0079	0.0273	0.0092	0.0063	0.0095	0.0123	0.0081	0.0088	0.0075	99.0000	99.0000
	Na5895′	TiO1	TiO2	<Fe>′	Fe3′	Fe4′	Fe5′	Fe6′	H'_A	H'_F	Balmer
	99.0000	99.0000	99.0000	−0.0077	−0.0076	−0.0056	−0.0001	99.0000	−0.0182	−0.0128	0.0669
	99.0000	99.0000	99.0000	0.0073	0.0062	0.0057	0.0069	99.0000	0.0167	0.0157	0.0322
ESO 079−003	$H\delta'_A$	$H\delta'_F$	CN1	CN2	Ca4227′	G-band	$H\gamma'_A$	$H\gamma'_F$	Fe4383′	Ca4455′	Fe4531′
	0.0844	0.1003	−0.0702	−0.0621	−0.0488	0.0374	−0.0167	−0.0015	−0.0261	−0.0104	0.0046
	0.0412	0.0566	0.0363	0.0407	0.0353	0.0345	0.0237	0.0370	0.0200	0.0231	0.0171
	C4668′	Hβ′	Fe5015′	Mg1	Mg2	Mgb	Fe5270′	Fe5335′	Fe5406′	Fe5709′	Fe5782′
	−0.0312	99.0000	−0.0210	−0.0207	−0.0304	0.0066	0.0036	−0.0031	−0.0045	−0.0133	−0.0302
	0.0176	99.0000	0.0149	0.0130	0.0136	0.0123	0.0161	0.0130	0.0109	0.0086	0.0087
	Na5895′	TiO1	TiO2	<Fe>′	Fe3′	Fe4′	Fe5′	Fe6′	H'_A	H'_F	Balmer
	−0.1599	−0.0060	−0.0064	0.0003	−0.0087	−0.0080	−0.0092	−0.0140	0.0319	0.0499	99.0000
	0.0134	0.0092	0.0068	0.0117	0.0116	0.0087	0.0107	0.0073	0.0243	0.0357	99.0000
ESO 234−053	$H\delta'_A$	$H\delta'_F$	CN1	CN2	Ca4227′	G-band	$H\gamma'_A$	$H\gamma'_F$	Fe4383′	Ca4455′	Fe4531′
	0.0187	0.0186	−0.0812	−0.0884	0.0115	−0.0055	0.0240	0.0170	−0.0288	0.0037	−0.0135
	0.0189	0.0241	0.0177	0.0207	0.0190	0.0172	0.0142	0.0140	0.0162	0.0257	0.0128
	C4668′	Hβ′	Fe5015′	Mg1	Mg2	Mgb	Fe5270′	Fe5335′	Fe5406′	Fe5709′	Fe5782′
	−0.0533	−0.1236	−0.0200	−0.0689	−0.0888	−0.0172	−0.0147	−0.0247	−0.0081	−0.0102	−0.0309
	0.0077	0.1248	0.0079	0.0068	0.0079	0.0098	0.0082	0.0081	0.0068	0.0079	0.0100
	Na5895′	TiO1	TiO2	<Fe>′	Fe3′	Fe4′	Fe5′	Fe6′	H'_A	H'_F	Balmer
	−0.2054	−0.0120	−0.0293	−0.0199	−0.0223	−0.0186	−0.0091	−0.0148	0.0217	0.0176	0.0779
	0.0176	0.0052	0.0068	0.0069	0.0085	0.0074	0.0105	0.0078	0.0116	0.0133	0.1215
-1mm] ESO 311−012	$H\delta'_A$	$H\delta'_F$	CN1	CN2	Ca4227′	G-band	$H\gamma'_A$	$H\gamma'_F$	Fe4383′	Ca4455′	Fe4531′
	0.0259	0.0135	−0.0549	−0.0561	−0.0024	−0.0086	0.0290	0.0257	−0.0173	−0.0120	−0.0034
	0.0081	0.0099	0.0073	0.0087	0.0114	0.0074	0.0066	0.0075	0.0075	0.0073	0.0067
	C4668′	Hβ′	Fe5015′	Mg1	Mg2	Mgb	Fe5270′	Fe5335′	Fe5406′	Fe5709′	Fe5782′
	−0.0217	−0.0360	−0.0147	−0.0203	−0.0369	−0.0194	−0.0079	0.0014	−0.0086	99.0000	99.0000
	0.0043	0.0202	0.0046	0.0031	0.0029	0.0040	0.0058	0.0060	0.0050	99.0000	99.0000
	Na5895′	TiO1	TiO2	<Fe>′	Fe3′	Fe4′	Fe5′	Fe6′	H'_A	H'_F	Balmer
	99.0000	99.0000	99.0000	−0.0032	−0.0071	−0.0073	−0.0094	99.0000	0.0266	0.0201	0.0158
	99.0000	99.0000	99.0000	0.0037	0.0034	0.0028	0.0035	99.0000	0.0047	0.0057	0.0190
ESO 443−042	$H\delta'_A$	$H\delta'_F$	CN1	CN2	Ca4227′	G-band	$H\gamma'_A$	$H\gamma'_F$	Fe4383′	Ca4455′	Fe4531′
	−0.0127	−0.0585	−0.0100	−0.0020	0.0256	0.0183	0.0026	−0.0377	−0.0231	−0.0204	−0.0176
	0.0279	0.0362	0.0269	0.0406	0.0481	0.0288	0.0197	0.0304	0.0277	0.0233	0.0173
	C4668′	Hβ′	Fe5015′	Mg1	Mg2	Mgb	Fe5270′	Fe5335′	Fe5406′	Fe5709′	Fe5782′
	−0.0017	0.0051	−0.0310	−0.0027	0.0025	−0.0328	−0.0045	−0.0181	−0.0110	99.0000	99.0000
	0.0135	0.0735	0.0120	0.0094	0.0113	0.0161	0.0139	0.0139	0.0158	99.0000	99.0000
	Na5895′	TiO1	TiO2	<Fe>′	Fe3′	Fe4′	Fe5′	Fe6′	H'_A	H'_F	Balmer
	99.0000	99.0000	99.0000	−0.0116	−0.0150	−0.0139	−0.0237	99.0000	−0.0055	−0.0479	0.0008
	99.0000	99.0000	99.0000	0.0081	0.0085	0.0064	0.0125	99.0000	0.0136	0.0232	0.0334

ESO 512−012	$H\delta'_A$	$H\delta'_F$	CN1	CN2	Ca4227′	G-band	$H\gamma'_A$	$H\gamma'_F$	Fe4383′	Ca4455′	Fe4531′
	0.0183	0.0361	−0.0314	−0.0026	0.0281	0.0003	0.0162	−0.0163	−0.0105	−0.1033	0.0659
	0.0308	0.0672	0.0353	0.0361	0.0417	0.0424	0.0304	0.0311	0.0482	0.0347	0.0305
	C4668′	$H\beta'$	Fe5015′	Mg1	Mg2	Mgb	Fe5270′	Fe5335′	Fe5406′	Fe5709′	Fe5782′
	−0.0121	0.0173	0.0245	0.0116	0.0432	0.0003	−0.0227	0.0088	0.0142	99.0000	99.0000
	0.0151	0.0498	0.0256	0.0150	0.0241	0.0208	0.0252	0.0178	0.0239	99.0000	99.0000
	Na5895′	TiO1	TiO2	<Fe>′	Fe3′	Fe4′	Fe5′	Fe6′	H'_A	H'_F	Balmer
	99.0000	99.0000	99.0000	−0.0073	−0.0083	−0.0026	−0.0038	99.0000	0.0167	0.0095	0.0348
	99.0000	99.0000	99.0000	0.0115	0.0194	0.0169	0.0152	99.0000	0.0182	0.0397	0.0259